Communal pairing in Fermi gases with attractive interactions

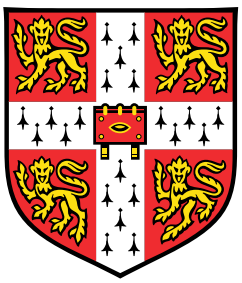

Darryl Foo Chuan Wei

This thesis is submitted for the degree of Doctor of Philosophy

Churchill College

August 2020

Declaration

This thesis is the result of my own work and includes nothing which is the outcome of work done in collaboration except as declared in the Preface and specified in the text. It is not substantially the same as any that I have submitted, or, is being concurrently submitted for a degree or diploma or other qualification at the University of Cambridge or any other University or similar institution except as declared in the Preface and specified in the text. I further state that no substantial part of my thesis has already been submitted, or, is being concurrently submitted for any such degree, diploma or other qualification at the University of Cambridge or any other University or similar institution except as declared in the Preface and specified in the text. It contains fewer than 60000 words including appendices, bibliography, footnotes, tables and equations.

Darryl Foo Chuan Wei
August 2020

Abstract

Darryl Foo Chuan Wei

Communal pairing in Fermi gases with attractive interactions

Weak attractive interactions in a spin-balanced fermion gas are known to induce a Cooper pairing instability where the fermion pairs have zero net momentum, leading to BCS superconductivity. Extensions for spin-imbalanced systems include breached superfluids, Fulde–Ferrell–Larkin–Ovchinnikov theory, and pair density wave theory. We propose a further extension of a superconducting state, dubbed a communal pairing state, whose underlying components are superpositions of Cooper pairs that share minority-spin fermions. This state includes correlations between all available fermions on both Fermi surfaces and is shown to be energetically favourable to the Fulde-Ferrell-Larkin-Ovchinnikov state. Our numerical quantum Monte Carlo study of finite spin-imbalanced systems provides clear evidence of the existence of such exotic pairing states. In spin-balanced systems, temporal fluctuations of the order parameter promote communal pairing, leading to a widening in momentum space of the superconducting gap and a decrease of the chemical potential.

Preface

The first chapter of this thesis provides an introduction to the field of attractively interacting fermion gases with a focus on various superconducting theories, followed up in the second chapter with the pertinent background theory of two-fermion scattering in 2D, two-fermion scattering on top of a Fermi surface, many-body superconducting theories and numerical Quantum Monte Carlo techniques. The last chapter presents a summary of the work done to this point and a roadmap of future work. Intermediate chapters contain work that is in preparation for submission or has been submitted for peer review as follows:

Chapter 3: T. M. Whitehead, D. C. W. Foo and G. J. Conduit (2019) [1]

Chapter 4: D. C. W. Foo and G. J. Conduit (2019) [2]

Chapter 5: D. C. W. Foo and G. J. Conduit (2020) [3]

I hereby declare that except where specific reference is made to the work of others, the contents of this thesis are original and have not been submitted in whole or in part for consideration for any other degree or qualification in this, or any other university. This thesis is my own work and contains nothing which is the outcome of work done in collaboration with others, except as specified in the text and this Preface. This thesis contains fewer than 60000 words including appendices, bibliography, footnotes, tables and equations.

This thesis was completed with support from the National University of Singapore and the Cambridge Trust.

Darryl Foo Chuan Wei
August 2020

Table of contents

1 Introduction **1**

1.1 BCS theory . . . 2
1.2 FFLO theory . . . 2
1.3 Communal superconductivity . . . 3
1.4 Numerical study . . . 4
1.5 Correction to spin-balanced systems . . . 5

2 Background theory **7**

2.1 2D scattering theory . . . 7
2.2 Cooper problem in a 2DFG . . . 9
2.2.1 Spin-balanced . . . 9
2.2.2 Spin-imbalanced . . . 10
2.3 Many-body superconducting theory . . . 14
2.3.1 Spin-balanced (BCS) . . . 14
2.3.2 Spin-imbalanced (FFLO) . . . 15
2.4 Quantum Monte Carlo . . . 16
2.4.1 Pseudopotential . . . 17
2.4.2 Variational Monte Carlo . . . 17
2.4.3 Diffusion Monte Carlo . . . 18
2.4.4 Heavy-tailed statistics . . . 20

3 Communal pairing theory **23**

4 Quantum Monte Carlo **29**

4.1 Method . . . 29
4.1.1 Overview . . . 29
4.1.2 Trial wavefunction . . . 30
4.1.3 Expectation values . . . 31
4.1.4 Simulation setup and convergence . . . 32
4.2 Results . . . 32

4.2.1 Spin-balanced BCS state . . . 32
4.2.2 Spin-imbalanced superconducting state . . . 33
4.2.3 Simulation parameters . . . 39
4.3 Conclusions . . . 41

5 Quantum fluctuations **43**
5.1 Quantum action . . . 44
5.2 Decoupling in a single channel . . . 45
5.2.1 Static single channel . . . 47
5.2.2 Oscillating single channel . . . 48
5.3 Multiple channels . . . 49
5.3.1 Static channels . . . 49
5.3.2 Finite Ω plasma . . . 50
5.3.3 Optimizing N_q . . . 51
5.3.4 Adding gap fluctuations . . . 52
5.3.5 Connection to BEC-BCS crossover . . . 53
5.4 Discussion and conclusions . . . 54

6 Concluding remarks **57**

References **59**

Chapter 1

Introduction

Condensed matter physics concerns itself primarily with the description of systems composed of vast numbers of quantum objects, a broad category encompassing things as mundane and everyday as solid metals to systems that cannot exist outside a laboratory, such as optically trapped cold atom gases. One of the successes of the field has been the description of the phenomenon of superconductivity by Bardeen, Cooper, and Schrieffer (BCS) in 1957 [4], more than 45 years after its first experimental observation by Onnes in 1911 [5, 6]. While only applicable for a certain class of systems, specifically those with an equal number of spin-up and spin-down fermions, BCS theory nevertheless remains a significant milestone in our understanding of condensed matter systems and numerous extensions have been considered in the 60 years hence. For example, Fulde and Ferrell (FF) [7], and Larkin and Ovchinnikov (LO) [8] would take the central idea of pairing fermions and apply it to spin-imbalanced systems, where the Fermi surfaces have different sizes, resulting in Cooper pairs with a net momentum and thus a spatial modulation of the superconducting gap. However, unlike with BCS theory that was preceded by an experimental result, observation of superconducting states in spin-imbalanced systems remains an experimental challenge despite considerable effort across a wide range of physical systems [9–17]. Nevertheless, the ongoing increase in computing speed and power has made it possible, not to mention increasingly easy, to simulate many-body quantum systems, affording us a fresh avenue of investigation into the pairing structure of these exotic systems.

This chapter will serve as a general and largely qualitative introduction to the foundational ideas underpinning both the well established BCS and FFLO theories and our novel communal pairing theory, which takes traditional FFLO theory as a base and considers additional degrees of variational freedom to search for a better description of the ground state. These additional degrees of freedom, $N_\uparrow$ and $N_\downarrow$, which we have dubbed communal pairing indices, denote the number of opposite spin fermions a particular fermion has nontrivial superconducting correlations with. For example, $N_\uparrow = 3$ means every down-spin fermion is correlated with 3 up-spin fermions. FFLO theory is recovered at $N_\uparrow = N_\downarrow = 1$ and so contained within our generalised variational space, yet we will find that the system energy is minimised by non-unit values at general spin-imbalance, with their ratio being equal to the ratio of the densities of states at the respective Fermi levels, $N_\uparrow/N_\downarrow = \nu_\uparrow/\nu_\downarrow$. We will also briefly introduce the

numerical quantum Monte Carlo techniques used to verify communal pairing theory and mention the correction to spin-balanced systems that arises from communal pairing considerations.

The next chapter will cover in more quantitative detail the essential background theory of 2D few-particle scattering, the Cooper problem in a 2D Fermi gas, and recapitulate the key results of BCS and FFLO theory and the quantum Monte Carlo algorithms. Chapters 3, 4 and 5 will in turn look at the theoretical framework of communal pairing theory, its numerical validation, and its extension to spin-balanced systems. Concluding remarks are presented in Chapter 6.

1.1 BCS theory

BCS theory was the first microscopic theory of superconductivity [4], precipitated by Cooper's observation that fermions on the Fermi surface are unstable against pairing of one up-spin fermion with one down-spin fermion when under the influence of any arbitrarily weak attractive interaction [18]. Cooper originally considered systems with equal numbers of spin up and spin down fermions, a condition that was maintained in the development of BCS theory. These papers considered only the particle-particle (pairing) channel and defined a homogenous isotropic superconducting order parameter proportional to the critical temperature. Later work by Gor'kov and Melik-Barkhudarov [19] included the effects of excitations in the particle-hole (screening) channel, so-called induced interactions, resulting in a reduction of the superconducting critical temperature by a factor of $(4e)^{1/3}$ in 3D, with later work by others showing similar reductions in lower dimensional systems [20, 21]. Despite these induced interactions working to suppress the onset of superconductivity, the fact that a pairing instability certainly exists did not change.

1.2 FFLO theory

Fulde and Ferrell (FF) [7], and separately Larkin and Ovchinnikov (LO) [8] extended BCS theory by considering systems with imbalanced spin populations and showing under what circumstances the formation of Cooper pairs is energetically favourable. FF theory in its initial form was concerned with a modulated gap parameter comprised of a single plane wave while LO theory considered a time-reversal symmetric gap parameter, with later extensions considering more general crystalline structure of the gap [22]. These would later collectively be called FFLO theory.

FFLO type superconductivity has been claimed to have been observed in heavy fermion systems [9], organic superconductors [13–15] and atomic ensembles in optical lattices [11, 12], though not all the experimental evidence gathered so far has been definitive and only a subset of materials that are superconducting when spin-balanced are predicted to exhibit FFLO superconductivity.

More recently, FFLO type superconductivity has come under the umbrella term of pair density wave superconductivity [23–27] which has in common a modulation of the superconducting order parameter but differs in its physical origin, with FFLO theory being a specific subset of pair density wave theory that arises specifically from a spin imbalance, whatever the cause of that spin imbalance may be. This

thesis will therefore continue to refer to FFLO theory as it is concerned with the effects of the spin imbalance.

Other potential pairing states in spin-imbalanced Fermi gases include the breached superfluid [28–31], which involves fermions of both species at the Fermi momentum of the minority spin-species forming pairs of zero net momentum, with the higher momentum states of the majority spin-species not interacting, and systems that have exceeded the Chandrasekhar-Clogston limit [32–35], where the interaction strength is high enough to promote members of the minority species up to the Fermi level of the majority species to form pairs of zero net momentum. Both these states have obvious experimental signatures when compared to FFLO type states when one considers the expected occupation numbers in momentum space, which may be measured experimentally from time-of-flight experiments and numerically from measuring the momentum density.

1.3 Communal superconductivity

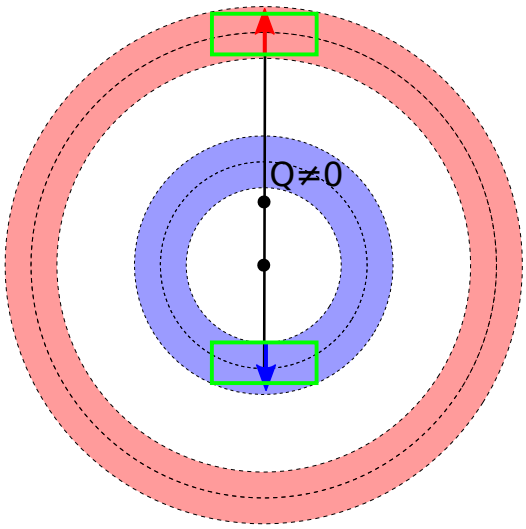

Fig. 1.1 Schematic of the potential pairing states of a spin-imbalanced Fermi gas. States within one Debye wavevector of the Fermi wavevector are shown for the majority (red) and minority (blue) species, with a particular pair of fermions highlighted with arrows. The green boxes show the states that are connected by a single scattering event to the highlighted pair. A complete tiling of the minority surface by such boxes will not cover the majority surface.

Despite the success of these theories, the formation of spin-singlet Cooper pairs in a spin-imbalanced fermion gas is limited by the minority species, leaving a potentially large fraction of the majority species not contributing to the correlation energy via attractive interactions. This is shown in Fig. 1.1, where a single FFLO type pair is shown with its connected states bordered by a green box. It is clear that were enough pairs present to cover the minority Fermi surface, the majority surface would still be underutilised owing to having far more available states.

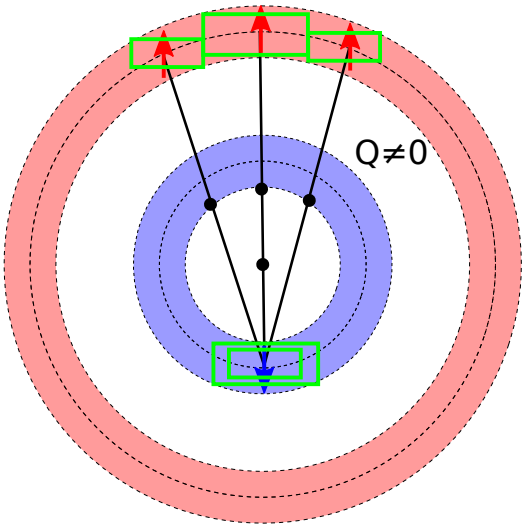

Fig. 1.2 Schematic of the potential pairing states of a spin-imbalanced Fermi gas. States within one Debye wavevector of the Fermi wavevector are shown for the majority (red) and minority (blue) species, with a particular communal set of fermions highlighted with arrows. The green boxes show the states that are connected by a single scattering event of the communal set. With more majority surface states used, greater correlation energy is possible.

Recent work by Conduit and Whitehead [36] sought to address this by considering multi-channel pairing with each minority species fermion paired with more than one majority species fermion. A potential multi-pairing setup is shown in Fig. 1.2. This, they argue, allows all the states on the majority-species Fermi surface to contribute to the correlation energy, and indeed the central result of [36] was that the optimal extended-pairing unit structure involves majority and minority-species fermions in the same ratio as the density of states at their respective Fermi surfaces. It should be noted that the basic components of the superconducting state are still Cooper pairs, only that the communal pairing language allows for superpositions of pairs and thus sharing of states between pairs, unlike in FFLO theory where each state has superconducting correlations with at most one other fermion state.

A follow-up manuscript by the aforementioned and myself [1] has considered the formation of a superconducting state using these "communal pairing" structures and came to a similar conclusion, that such a superconducting state is favoured over the FFLO state, stabilised by the additional variational freedom allowed by non-exclusive pairing. However, as with FFLO states, such a state currently lacks experimental evidence to support its existence. To use the results of a numerical Quantum Monte Carlo simulation to discern whether communal pairing states exist and how they relate to FFLO is thus another aim of the project.

1.4 Numerical study

This thesis therefore, in addition to the aforementioned analytical work, will approach the issue of spin-imbalanced fermion systems from an orthogonal perspective, using advanced Quantum Monte Carlo methods to simulate a generic, finite, spin-imbalanced system [2]. Extensive use will be made of the CASINO program [37] to perform numerical simulations of finite spin-imbalanced interacting fermion systems and thereby investigate the manner and extent of pairing in these systems. In order to

mitigate the sign problem, the simulations will be done in two phases using two different techniques, Variational Monte Carlo (VMC) and Diffusion Monte Carlo (DMC). DMC is more accurate than VMC but slower and more computationally intensive, and further suffers from being unable to alter the nodal structure of any proposed input trial wavefunction owing to the aforementioned sign problem. VMC on the other hand does not suffer from this particular drawback, being able to variationally change the nodal structure of its trial wavefunction. We will therefore first use VMC to determine a "good" trial wavefunction to later feed into DMC for further refinement and measurement of the state energy.

1.5 Correction to spin-balanced systems

In the coming chapters it will be shown that communal pairing theory makes use of the variational principle to assert itself as a strict improvement over FFLO theory as a description of the superconducting ground state of spin-imbalanced Fermi systems [1], an assertion backed up by numerical results [2]. A question naturally arises then as to whether such communal corrections have any impact on the BCS ground state of spin-balanced systems, and under what circumstances these corrections may be visible. In the zero temperature limit, quantum temporal fluctuations of the superconducting order parameter drive communal pairing and concomitant widening of the superconducting gap in momentum space, leading to a decrease in the chemical potential. This width increases with increasing interaction strength and the effect is more pronounced in 2D than in 3D, as fluctuations are stronger there. In the language of communal pairing indices, we indeed find from communal pairing theory that the optimal ratio of communal pairing indices $N_\uparrow/N_\downarrow = 1$ for a spin-balanced system [1, 2], but we can have $N_\uparrow N_\downarrow > 1$ due to fluctuations. This will be explored in Chapter 5 where we have taken $N_\uparrow = N_\downarrow = N_q$ for simplicity.

Chapter 2

Background theory

Having qualitatively introduced various theories, we will proceed now to a more quantitative description of systems of many attractively interacting fermions. We note from the outset that the large spin-imbalances to be studied here are more readily probed in cold atom ensembles in atomic lattices than in ordinary quantum matter and so aim towards a description suitable for such systems. This will be done in stages, beginning by first summarising the important results of scattering theory for two isolated particles in 2D and using the obtained results to construct a theory for two particles interacting on top of their respective Fermi surfaces, in analogy with the original Cooper problem [18] which was done for electrons in a metal. We will then provide brief outlines of the many body BCS and FFLO theories proper before moving on to a description of the numerical Quantum Monte Carlo techniques that will be used to simulate these many-fermion systems.

2.1 2D scattering theory

In order to solve the Cooper problem for a general 2D Fermi gas (2DFG), that is without resorting to introducing an upper limit in energy via the Debye energy, it is necessary to first obtain a relation between the interaction strength and the scattering length and effective range. This approach is necessary when dealing with, for example, cold atom gases which lack an accompanying ionic lattice through which phonons and thus a Debye energy may be introduced. We follow the derivation laid out in [38] where this was done in 3D and start with the Schrödinger equation for two fermions in their center of momentum frame in Hartree units,

$$(\nabla^2 + k^2)\psi(\mathbf{r}) = V(\mathbf{r})\psi(\mathbf{r}), \tag{2.1}$$

where the eigenenergy has been identified as $E \equiv \hbar^2 k^2/2m = k^2$ with $m = 1/2$ the reduced mass. $V(\mathbf{r})$ is the interaction potential and $\psi(\mathbf{r})$ is the spatial part of the 2-fermion wavefunction. We restrict our discussion to the spin-singlet channel and consider only spin-independent potentials. Outside the interaction region, where $V(\mathbf{r}) = 0$, the equation (2.1) admits plane wave solutions. Therefore, following

the prescription laid out in [39] we consider the asymptotic ansatz

$$\psi_{\mathbf{k}}(\mathbf{r}) \xrightarrow[r\to\infty]{} \mathrm{e}^{\mathrm{i}\mathbf{k}\cdot\mathbf{r}} + f_{\mathbf{k}',\mathbf{k}}\sqrt{\frac{1}{kr}}\mathrm{e}^{\mathrm{i}(kr+\pi/4)}, \tag{2.2}$$

consisting of an incident plane wave and a scattered cylindrical wave with scattering amplitude $f_{\mathbf{k}',\mathbf{k}}$, where $\mathbf{k}'$ defines the direction of the scattered wave and $|\mathbf{k}'| = |\mathbf{k}|$ for elastic scattering. The Lipmann-Schwinger equation may then be expressed in terms of the scattering amplitude as

$$\begin{aligned} f_{\mathbf{k}',\mathbf{k}} &= \frac{-1}{2\sqrt{2\pi}}\int \mathrm{d}^2 r \mathrm{e}^{-\mathrm{i}\mathbf{k}'\cdot\mathbf{r}} V(\mathbf{r})\psi_{\mathbf{k}}(\mathbf{r}) \\ &= \frac{-v(\mathbf{k}'-\mathbf{k})}{2\sqrt{2\pi}} + \lim_{\eta\to 0^+}\int \frac{\mathrm{d}^2 q}{(2\pi)^2}\frac{v(\mathbf{k}'-\mathbf{q})f_{\mathbf{q},\mathbf{k}}}{k^2-q^2+\mathrm{i}\eta}, \end{aligned} \tag{2.3}$$

where the lowercase $v(\mathbf{k})$ is used to denote the fourier transform of the interaction potential $V(\mathbf{r})$. The scattering amplitude can be related to the scattering phase shifts by decomposing a plane wave into a sum of incoming and outgoing cylindrical Hankel functions and applying the usual phase shift to the outgoing wave, $H_n^{(1)}(kr) \to \mathrm{e}^{2\mathrm{i}\delta_n}H_n^{(1)}(kr)$, where δ_n is the n-th order phase shift and the factor of two is conventional. It is a simple matter then to isolate the scattering amplitude as

$$\begin{aligned} \psi_{\mathbf{k}}(\mathbf{r}) - \mathrm{e}^{\mathrm{i}\mathbf{k}\cdot\mathbf{r}} &= f_{\mathbf{k}',\mathbf{k}}\sqrt{\frac{1}{kr}}\mathrm{e}^{\mathrm{i}(kr+\pi/4)} \\ &= \sum_{n=-\infty}^{\infty}\frac{\mathrm{i}^n}{2}\mathrm{e}^{\mathrm{i}n\theta}(\mathrm{e}^{2\mathrm{i}\delta_n}-1)H_n^{(1)}(kr). \end{aligned} \tag{2.4}$$

Low energy scattering is expected to have the s-term, that is the $n = 0$ term, dominate and so an approximate expression for the scattering amplitude may be found as

$$f_{\mathbf{k}',\mathbf{k}} \approx \frac{-\mathrm{i}}{\sqrt{2\pi}}(\mathrm{e}^{2\mathrm{i}\delta_0}-1) = \sqrt{\frac{2}{\pi}}\frac{1}{\cot\delta_0 - \mathrm{i}}, \tag{2.5}$$

where we have taken the asymptotic form of the zeroth-order Hankel function of the first kind in the infinite r limit, $H_0^{(1)}(kr) \to \sqrt{\frac{2}{\pi kr}}\mathrm{e}^{\mathrm{i}(kr-\pi/4)}$ as $r \to \infty$.

The cotangent of the lowest order phase shift has the expansion [40]

$$\cot\delta_0 \approx \frac{2}{\pi}\ln ka + \frac{1}{2\pi}r_{\mathrm{e}}^2 k^2, \tag{2.6}$$

where $a = (e^{\gamma}/2)a_{\mathrm{s}} \approx 0.89a_{\mathrm{s}}$ is a scaled version of the scattering length a_{s} with γ the Euler-Mascheroni constant and r_{e} is the effective range. Since the expansion is cylindrically symmetric up to this order, we can replace $f_{\mathbf{k}',\mathbf{k}}$ with f_k and rewrite the Lipmann-Schwinger equation (2.3) as

$$\frac{1}{v_0} = \frac{-1}{2\sqrt{2\pi}}\frac{1}{f_k} + \lim_{\eta\to 0^+}\int \frac{\mathrm{d}^2 q}{(2\pi)^2}\frac{1}{k^2-q^2+\mathrm{i}\eta}, \tag{2.7}$$

where we have assumed that $v(\mathbf{k})$ is also cylindrically symmetric and approximated by a top hat function with height v_0 over some finite range of momenta given by $1/l$ with l the extent of the interaction region and zero otherwise, and divided through by $f_k v_0$. In the limit of a contact interaction, $v(\mathbf{k}) = v_0$ for all momenta. By substituting in equations (2.5) and (2.6) and converting the integral over momentum states into one over energy, the equation becomes

$$\frac{1}{v_0} = \frac{-1}{2\pi}\ln ka - \frac{1}{8\pi}r_e^2 k^2 + \frac{\mathrm{i}}{4} - \lim_{\eta\to 0^+}\int \frac{\rho_{2D}(\varepsilon)\mathrm{d}\varepsilon}{2\varepsilon - E - \mathrm{i}\eta}, \tag{2.8}$$

where $\rho_{2D}(\varepsilon) = 1/2\pi$ is the density of states in energy in 2D for a fermion of one spin species, $2\varepsilon = q^2$ is the energy of a fermion pair and we reintroduce $E = k^2$ the eigenenergy of the original Schrödinger equation (2.1). Substituting in the value of $\rho_{2D}(\varepsilon)$ and making use of the Sokhotski-Plemelj theorem to perform the integration over ε from 0 to some upper bound E_u gives

$$\frac{1}{v_0} = \frac{-1}{2\pi}\ln ka - \frac{1}{8\pi}r_e^2 k^2 - \frac{1}{4\pi}\ln\frac{2E_u - E}{E}. \tag{2.9}$$

In phonon-mediated superconductors, E_u would be roughly the Debye energy plus the Fermi energy but in general 2DFGs, there may not be any obvious physical mechanism with which to introduce a cutoff, so the result is generically divergent. It will be shown in the following section however that when applied to Cooper pairing this divergence is exactly cancelled by another and the regularisation procedure is well defined.

2.2 Cooper problem in a 2DFG

2.2.1 Spin-balanced

Cooper was interested in the binding energy of a fermion pair above the Fermi surface with attractive interactions [18]. In the language used so far, the modulus of the binding energy is given by $|E_B| = 2E_F - E$ where E_F is the Fermi energy. For attractive interactions, the defining equation is

$$-\frac{1}{v_0} = \int_{E_F}^{E_u} \frac{\rho_{2D}(\varepsilon)\mathrm{d}\varepsilon}{2(\varepsilon - E_F) + |E_B|}, \tag{2.10}$$

where the effect of Pauli blocking is taken care of by setting the lower limit of the integral to be E_F. In conventional superconductors, the upper limit E_u is replaced by $E_F + \varepsilon_D$ with ε_D the Debye energy and provided $\varepsilon_D \ll E_F$, we obtain the relation

$$E_B = -2\varepsilon_D e^{2/\rho_{2D}v_0}. \tag{2.11}$$

For a 2DFG it is necessary to replace v_0 using the result of equation (2.9) giving

$$2\ln ka + \frac{1}{2}r_e^2 k^2 = \ln\frac{2E_F - |E_B|}{|E_B|}, \tag{2.12}$$

where as previously mentioned the divergence in the upper limit of the energy has been exactly cancelled. It should be noted here that we have made the identification $k^2 \equiv E = 2E_F + E_B$. For $E_B \ll E_F$, $k \approx k_F$ the Fermi wavevector and this equation is easily rearranged to give the binding energy in terms of the scattering length and effective range as

$$E_B \approx -\frac{2E_F}{1 + e^{\frac{1}{2}r_e^2 k_F^2} k_F^2 a^2}. \tag{2.13}$$

If $E_B \not\ll E_F$, equation (2.12) is transcendental and cannot be solved algebraically unless $r_e = 0$, in which case the equation is quadratic in E_B and the result is simply

$$E_B = -a^{-2}, \tag{2.14}$$

which is true for all physical scattering lengths a. The other solution is $E_B = -2E_F$ i.e. $E = 0$ which is only satisfied for general potentials and scattering lengths if there are no fermions present.

2.2.2 Spin-imbalanced

Self-consistent equation

The extension of this result to the spin-imbalanced case is straightforward, albeit lacking a simple analytic form. Unlike in the spin-balanced case, where the symmetry of the problem makes it convenient to work in energy, here it is necessary to work in momentum. Starting from Eq. (2.8), we split the integral over energy into a vanishing Cauchy principal value integral containing the pole at $\varepsilon = E/2$ and another well defined integral that we convert back into momentum space, obtaining

$$\frac{1}{v_0} = \frac{-1}{2\pi}\ln ka - \frac{1}{8\pi}r_e^2 k^2 - \int_{\sqrt{2}k}^{q_u} \frac{\mathrm{d}^2 q}{(2\pi)^2}\frac{1}{q^2 - k^2}. \tag{2.15}$$

We note that the only thing that has been done so far is a simple re-statement of the Lipmann-Schwinger equation to obtain the scattering potential v_0 in terms of the scattering length a, effective range r_e and an integral over momentum. As it stands, the equation still requires that the total energy of the fermion pair k^2 be evaluated in their center of momentum frame.

To find the binding energy of a Cooper pair in a spin-imbalanced system, we introduce two Fermi energies, $E_{F,\uparrow}$ and $E_{F,\downarrow}$, and two Fermi wavevectors, $k_{F,\uparrow}$ and $k_{F,\downarrow}$, for the up and down spin species respectively. We state here without loss of generality that we take the majority species to be spin-up and the minority species to be spin-down. We also parametrise the momenta of the fermions as $\mathbf{Q} + \mathbf{q}$ and $\mathbf{Q} - \mathbf{q}$, so that their total momenta is $2\mathbf{Q}$ and total energy is $q^2 + Q^2$. This allows us to express the

Cooper pairing equation as

$$-\frac{1}{v_0} = \int_A \frac{\mathrm{d}^2 q}{(2\pi^2)} \frac{1}{q^2 - k^2}, \tag{2.16}$$

where $k^2 = E_{\mathrm{F},\uparrow} + E_{\mathrm{F},\downarrow} - |E_{\mathrm{B}}| - Q^2$ is the energy of the interacting fermions in their center of momentum frame and the integration is over a modified region A of momentum space defined by $|\mathbf{Q}+\mathbf{q}| > k_{\mathrm{F},\uparrow}$ and $|\mathbf{Q}-\mathbf{q}| > k_{\mathrm{F},\downarrow}$, which is such that the fermion pair has the same total momentum with neither spin-species beneath their respective Fermi surfaces. We note that the momentum integrals in equations (2.15) and (2.16) have the same form and divergence characteristics, differing only in the region of integration near the Fermi surfaces, therefore the logarithmic divergences cancel, giving us the final self-consistency equation

$$2\pi \ln ka + \frac{\pi}{2} r_{\mathrm{e}}^2 k^2 = \int_A^{q=\sqrt{2}k} \frac{\mathrm{d}^2 q}{q^2 - k^2}. \tag{2.17}$$

The limits of the integral are such that the integrand is purely positive and finite so the expression is properly regularised and converges and we can solve for k^2 numerically to obtain the binding energy. As the lower limit A is a function of Q, so is k and therefore E_{B}.

Optimal pair momentum

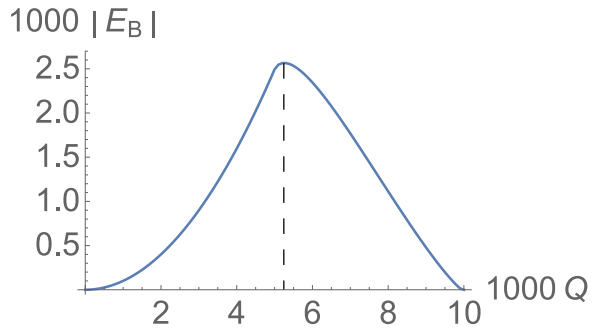

Fig. 2.1 Graph of binding energy $|E_{\mathrm{B}}|$ against pair momentum Q for fixed spin-imbalance $k_{\mathrm{F},\uparrow} - k_{\mathrm{F},\downarrow} = 1/100$. The binding energy (solid blue) exhibits a maximum at a value $Q_{\max} \approx 0.00525$, shown by the dotted black line. This is approximately 5% above $Q_0 = 0.005$, the pair momentum for fermions on opposite sides of their respective Fermi surfaces. $E_{\mathrm{F},\uparrow} + E_{\mathrm{F},\downarrow} = 1$, $a = 10$, $r_{\mathrm{e}} = 0$.

The self-consistency equation (2.17) can be solved numerically to obtain the optimal value of Q for which the binding energy is extremised for a particular spin-imbalance. An example curve is shown in Fig. 2.1 for an interaction with $a = 10$ and $r_{\mathrm{e}} = 0$ for a spin imbalance such that $k_{\mathrm{F},\uparrow} - k_{\mathrm{F},\downarrow} = 1/100$ in units where $E_{\mathrm{F},\uparrow} + E_{\mathrm{F},\downarrow} = 1$.

The binding energy is shown to grow in magnitude before decreasing with increasing Q. This is because at $Q = 0$ the lower limit A excludes regions where the integrand is large and includes regions where the integrand is small, leading to a lower binding energy. As Q increases, more of the strongly contributing regions and less of the weakly contributing regions are included, leading to an initial increase in $|E_{\mathrm{B}}|$. Over the range $0 < Q < \frac{1}{2}(k_{\mathrm{F},\uparrow} - k_{\mathrm{F},\downarrow})$, the lower limit A may be defined solely by the first constraint, $|\mathbf{Q}+\mathbf{q}| > k_{\mathrm{F},\uparrow}$, an off-center circle of radius $k_{\mathrm{F},\uparrow}$. As Q increases further however, the second constraint, $|\mathbf{Q}-\mathbf{q}| > k_{\mathrm{F},\downarrow}$, is no longer a subset of the first and a second circle of radius $k_{\mathrm{F},\downarrow}$ begins to be excluded from the integration region, causing the value of the integral to decrease and

thus the value of $|E_B|$ to decrease. This happens close to, but not exactly at, $Q_0 = \frac{1}{2}(k_{F,\uparrow} - k_{F,\downarrow})$, the pair momentum for two fermions at opposite sides of their respective Fermi surfaces. Nevertheless this value Q_0 is a useful analytic approximation for Q_{max} that itself lacks an analytic form. Q_0 also has an obvious physical interpretation of two fermions at opposite sides of their respective Fermi surfaces, or equivalently the minimum Q possible when the fermion energies are individually minimised.

Bounds on the binding energy

The regularisation of the integral may be visualised as in Fig. 2.2, which is drawn with $Q = Q_0$ for two different values of spin-imbalance. The red and blue circles indicate the majority and minority Fermi surfaces respectively, and are therefore concentric. The black cross is the midpoint between the left-most point of the red circle and the right-most point of the blue, **Q**, the origin of integrations over **q** with $Q = Q_0$. The green, dotted and dot-dashed circles are centered on the black cross. Here, the region A begins from the majority spin Fermi surface and goes to infinity, while the limits of the integral in equation (2.15) start approximately at the green circle and go to infinity, so that the net region of integration is from the red circle to the green circle. The region of integration is clearly finite for all spin imbalances and the integrand is positive and finite, so the divergence has been regularised appropriately. As the circles are not concentric, the integral lacks an analytic form in general. It bears mentioning for completeness that the green circles in the figure overestimate the true radius of $\sqrt{2}k$ by neglecting the contribution of E_B to k, essentially neglecting self-consistency.

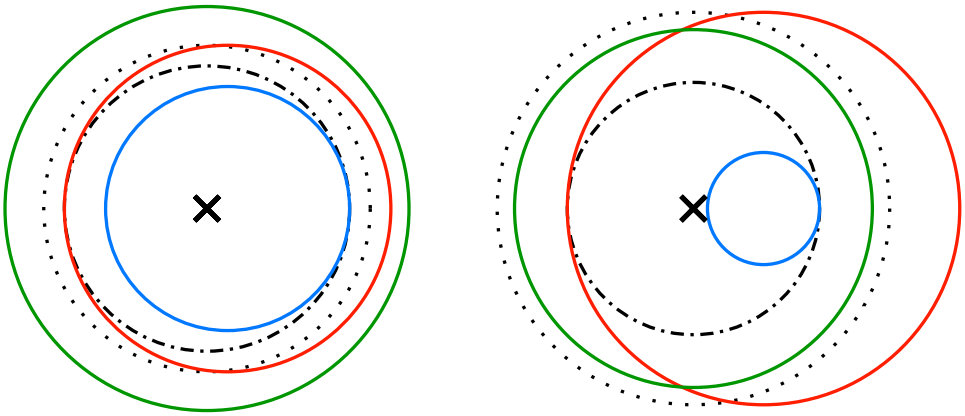

Fig. 2.2 Limits of integration in momentum space for mild (left) and severe (right) spin imbalance. Fermi surfaces are shown for the majority (red) and minority (blue) spin species, with the $\times$ denoting **Q**, the origin of integrations over **q** with $Q = Q_0$. The majority Fermi surface is the true lower limit of the q-space integration of the Cooper problem, with approximate lower limits shown for obtaining the lower (dotted) and upper (dash-dotted) bounds of E_B. An approximate upper limit is shown (green) with radius $\sqrt{2(k^2 + |E_B|)}$; the true upper limit has a smaller radius.

It is clear from the diagram that with increasing spin-imbalance, the radius of the green circle decreases while that of the red circle increases, decreasing the value of the integral and thus decreasing

the magnitude of the binding energy. Fixing the total fermion number and therefore the total area of the red and blue circles, we can vary the spin-imbalance to find that when $k_{\mathrm{F},\uparrow}/k_{\mathrm{F},\downarrow} = \frac{1}{3}(2\sqrt{13}+1)$, the green circle intersects the red circle and thus regions of the integral begin to contribute negatively.

Bounds on the value of the integral may be found by replacing the shifted red circle defining the lower limit with another circle concentric with the green circle. A lower bound is found by maintaining the radius of the circle and shifting it to be centered on $q = 0$, represented by dotted circles in Fig. 2.2, while an upper bound is similarly found by finding the largest concentric circle contained within the red circle, shown as dotted-dashed circles. As can be seen in the right hand diagram of Fig. 2.2, a severe spin-imbalance can lead to a lower limit circle larger than the upper limit, so the lower bound on the magnitude of the binding energy is negative. This corresponds geometrically to when the green circle is the same radius as the red circle and occurs at a spin-imbalance $k_{\mathrm{F},\uparrow}/k_{\mathrm{F},\downarrow} = \sqrt{2}+1$. Unlike with the dotted circle, the dotted-dashed circle never exceeds the radius of the green circle and so the upper bound is always positive.

If the total number of fermions is held constant so that compared to the spin balanced case, $E_{\mathrm{F},\uparrow} + E_{\mathrm{F},\downarrow} = 2E_{\mathrm{F}}$, we can evaluate both of these expressions for $Q = Q_0$ and $r_{\mathrm{e}} = 0$ to give the bounds of the binding energy in the spin-imbalanced case as

$$a^{-2} - (E_{\mathrm{F},\uparrow} - E_{\mathrm{F},\downarrow}) - Q_0^2 < |E_{\mathrm{B}}| < a^{-2}, \tag{2.18}$$

so the binding energy is always of a smaller magnitude than in the spin-balanced case. For decreasing strength of the scattering potential, a increases and so for a general spin imbalance, and equivalently a general $E_{\mathrm{F},\uparrow} - E_{\mathrm{F},\downarrow}$, it is possible that the lower bound is negative, as previously mentioned; as such the present analysis does not suggest a pairing instability in a spin-imbalanced system for all interaction strengths or scattering lengths a, in contrast with what has been shown in the spin-balanced system.

Paramagnetic suppresion

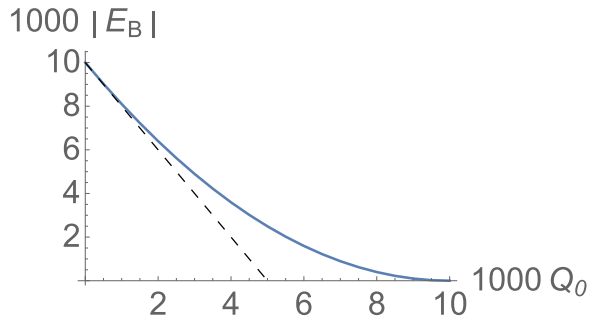

Fig. 2.3 Graph of binding energy $|E_{\mathrm{B}}|$ at $Q = Q_0$ against approximately optimal pair momentum Q_0 for increasing spin-imbalance. Binding energy (solid blue) is seen to decrease dramatically with increasing spin-imbalance. The small Q_0 behaviour is shown to match with the theoretical prediction (dashed black) to first order. $E_{\mathrm{F},\uparrow} + E_{\mathrm{F},\downarrow} = 1$, $a = 10$, $r_{\mathrm{e}} = 0$.

Approximating the optimal pairing momentum as $Q = Q_0$ and taking this as the measure of spin-imbalance, the self-consistent equation (2.17) may be integrated numerically to obtain the binding energy as a function of spin-imbalance. Example results are shown in Fig. 2.3 for an interaction with $a = 10$ and $r_{\mathrm{e}} = 0$ in units where $E_{\mathrm{F},\uparrow} + E_{\mathrm{F},\downarrow} = 1$. The magnitude of the binding energy $|E_{\mathrm{B}}|$ is plotted for

increasing Q_0, shown as a solid blue line. A sharp decrease in the magnitude of the binding energy is seen as the spin-imbalance and Q_0 increase, as is expected from considerations of the movement of integration limits as seen in Fig. 2.2. Using the expression of the lower bound to approximate the variation of $|E_B|$ with Q_0, for $Q_0 \ll k_F$ with k_F the fermi wavevector of the spin-balanced system with the same number of fermions, the lower bound may be expanded in small Q_0 as $|E_B| = a^{-2} - 2k_F Q_0 + \mathcal{O}(Q_0^2)$ which in the units used to obtain the figure implies an initial gradient of -2. Such a gradient is shown by a dashed black line indicating a good agreement for small Q_0 between the real curve and the approximation from the lower bound. The effect of using the crude approximation is evident on considering higher order terms, as the coefficient of the Q_0^2 term obtained from the lower bound is negative, implying that the blue curve is expected to fall below the dashed black line. Instead, the blue curve decreases more gradually, consistent with having used a lower bound for approximation.

2.3 Many-body superconducting theory

The preceding sections built up a theory of fermion pairing in a few-fermion context, working first with only two fermions before considering the effect of a (non-interacting) filled Fermi sea under those two fermions. Such a picture, while affording qualitative insight into the pairing instability, is nevertheless an oversimplification and so we move now into a true many-body description of attractively interacting Fermion gases.

2.3.1 Spin-balanced (BCS)

The many-body Hamiltonian for attractive point interactions in a spin-balanced fermion gas is

$$H = \sum_{\mathbf{k},\sigma} \varepsilon_{\mathbf{k}} c^\dagger_{\mathbf{k},\sigma} c_{\mathbf{k},\sigma} - g \sum_{\mathbf{k},\mathbf{k}',\mathbf{Q}} c^\dagger_{\mathbf{k}+\mathbf{Q},\uparrow} c^\dagger_{-\mathbf{k}+\mathbf{Q},\downarrow} c_{-\mathbf{k}'+\mathbf{Q},\downarrow} c_{\mathbf{k}'+\mathbf{Q},\uparrow}, \tag{2.19}$$

where $\mathbf{k}$, $\mathbf{k}'$ and $\mathbf{Q}$ are wavevectors, $\sigma \in \{\uparrow,\downarrow\}$ is the spin index, $\varepsilon_{\mathbf{k},\sigma}$ is the single-particle dispersion, $c^\dagger_{\mathbf{k},\sigma}$ ($c_{\mathbf{k},\sigma}$) is an fermion creation (annihilation) operator and $g > 0$ is the strength of the (attractive) contact interaction. We can however further simplify this by noting that based on the results of the few particle analysis above, we expect the dominant role to be played by fermion pairs with zero net momentum. We therefore set $\mathbf{Q} = 0$ and thus obtain the BCS Hamiltonian

$$H_{\mathrm{BCS}} = \sum_{\mathbf{k},\sigma} \varepsilon_{\mathbf{k}} c^\dagger_{\mathbf{k},\sigma} c_{\mathbf{k},\sigma} - g \sum_{\mathbf{k},\mathbf{k}'} c^\dagger_{\mathbf{k},\uparrow} c^\dagger_{-\mathbf{k},\downarrow} c_{-\mathbf{k}',\downarrow} c_{\mathbf{k}',\uparrow}. \tag{2.20}$$

The effect of the interaction is to mix states of zero net momentum and so , following after BCS [4], the ansatz wavefunction is chosen to be

$$|\Psi_{\mathrm{BCS}}\rangle = \prod_{\mathbf{k}} \left(u_{\mathbf{k}} + v_{\mathbf{k}} c^\dagger_{\mathbf{k},\uparrow} c^\dagger_{-\mathbf{k},\downarrow} \right) |\mathrm{VAC}\rangle, \tag{2.21}$$

where $u_{\mathbf{k}}$ and $v_{\mathbf{k}}$ are variational parameters such that $|u_{\mathbf{k}}|^2 + |v_{\mathbf{k}}|^2 = 1$ and $|\text{VAC}\rangle$ is the vacuum state. This wavefunction is analogous to the coherent states used in quantum optics and in studies of superfluids. While introduced by BCS as an ansatz, it can be shown to be the exact ground state solution of the BCS Hamiltonian. Minimizing the free energy $F = H - \mu N$, where N is the total particle number, with respect to the variational parameters leads to the equations

$$|u_{\mathbf{k}}|^2 = \frac{1}{2}\left(1 + \frac{\xi_{\mathbf{k}}}{E_{\mathbf{k}}}\right), \quad |v_{\mathbf{k}}|^2 = \frac{1}{2}\left(1 - \frac{\xi_{\mathbf{k}}}{E_{\mathbf{k}}}\right), \tag{2.22}$$

where $E_{\mathbf{k}} = \sqrt{\xi_{\mathbf{k}}^2 + |\Delta|^2}$ and the gap Δ is defined by the gap equation

$$\Delta \equiv -g\sum_{\mathbf{k}}\langle c_{\mathbf{k},\uparrow}c_{-\mathbf{k},\downarrow}\rangle = g\sum_{\mathbf{k}}\frac{\Delta}{2E_{\mathbf{k}}}. \tag{2.23}$$

We can then divide through by the constant $g\Delta$ to obtain

$$\frac{1}{g} = \int \frac{A\mathrm{d}^2k}{(2\pi)^2}\frac{1}{2E_{\mathbf{k}}}, \tag{2.24}$$

where A is the system area and we have now made explicit that the system being discussed is in 2D. This equation is similar in form to Eq. 2.10 and we can substitute in the result of Eq. 2.9 to obtain

$$\ln \kappa a = \int_0^\infty \frac{\mathrm{d}\varepsilon}{2\sqrt{(\varepsilon-\mu)^2 + |\Delta|^2}} - \int_{\kappa^2}^\infty \frac{\mathrm{d}\varepsilon}{2\varepsilon - \kappa^2}, \tag{2.25}$$

where we have assumed from the outset that $r_\mathrm{e} = 0$, identified g with the potential $-v_0$ from the previous section and for the sake of clarity have relabelled the pair energy from k^2 to κ^2. As in the few particle case, the fermion pair energy κ^2 cancels out and the result for the gap is

$$|\Delta| = \frac{\sqrt{2\mu}}{a}. \tag{2.26}$$

The scaling of the gap with scattering length is thus quantitatively different to that of the few fermion analysis, being proportional to the inverse rather than the inverse square. This factor of 2 difference in the exponent is typically explained as a manifestation of Pauli blocking when going from the few to many-fermion analysis and can be seen in the well known results for solid-state superconductors in 3D, where the binding energy is $|E_{B,3D}| = 2\varepsilon_\mathrm{D}\mathrm{e}^{-\frac{2}{g\nu_\mathrm{F}}}$ and that for the gap is $\Delta_{3D} = 2\varepsilon_\mathrm{D}\mathrm{e}^{-\frac{1}{g\nu_\mathrm{F}}}$ where ν_F is the density of states at the Fermi surface.

2.3.2 Spin-imbalanced (FFLO)

Like with the few-particle analysis with two interacting fermions on top of a filled non-interacting Fermi sea, the extension from spin-balanced to spin-imbalanced brings with it a wealth of discussion and theory, as in [22] and the references therein. However, for our discussion the salient point is that the gap

parameter acquires a spatial modulation. Consider the original Hamiltonian in Eq. 2.19; the effect of the interaction is to mix states of fixed momentum. We construct such an ansatz state as

$$|\Psi\rangle = \sum_{N,\mathbf{Q}} c_{N,\mathbf{Q}} |N,\mathbf{Q}\rangle , \tag{2.27}$$

where N is even and the state $|N,\mathbf{Q}\rangle$ contains $N/2$ fermion pairs of momentum $\mathbf{k}+\mathbf{Q}$ and $-\mathbf{k}+\mathbf{Q}$ for the majority and minority spin species respectively and the sum over N implies an integration over $\mathbf{k}$. Anticipating the emergence of spatial modulation of the gap, we define

$$\Delta(\mathbf{r}) \equiv -g\langle \psi_\uparrow(\mathbf{r})\psi_\downarrow(\mathbf{r})\rangle \tag{2.28}$$

where $\psi_\sigma(\mathbf{r}) \equiv \sum_{\mathbf{k}} e^{i\mathbf{k}\cdot\mathbf{r}} c_{\mathbf{k},\sigma}$. This is related to the previously defined BCS gap by the relation $\Delta = \frac{1}{A}\int d\mathbf{r}\Delta(\mathbf{r})$. With the proposed ansatz, this gap function then becomes

$$\begin{aligned}
\Delta(\mathbf{r}) &= -g \sum_{N,\mathbf{Q}} c^*_{N,\mathbf{Q}} c_{N+2,\mathbf{Q}} \langle N,\mathbf{Q}| \psi_\uparrow(\mathbf{r})\psi_\downarrow(\mathbf{r}) |N+2,\mathbf{Q}\rangle \\
&= -g \sum_{N,\mathbf{Q}} c^*_{N,\mathbf{Q}} c_{N+2,\mathbf{Q}} e^{2i\mathbf{Q}\cdot\mathbf{r}} \langle N,\mathbf{Q}| \psi_\uparrow(0)\psi_\downarrow(0) |N+2,\mathbf{Q}\rangle \\
&= \sum_{\mathbf{Q}} \Delta_{\mathbf{Q}} e^{2i\mathbf{Q}\cdot\mathbf{r}}
\end{aligned} \tag{2.29}$$

where we have defined $\Delta_{\mathbf{Q}} \equiv -g\sum_N c^*_{N,\mathbf{Q}} c_{N+2,\mathbf{Q}} \langle N,\mathbf{Q}| \psi_\uparrow(0)\psi_\downarrow(0) |N+2,\mathbf{Q}\rangle$, and it remains to minimise the free energy with respect to the $c_{N,\mathbf{Q}}$. BCS theory is recovered if the state $|\Psi\rangle$ is only constructed from zero net momentum pair states so that $\Delta(\mathbf{r}) = \Delta_0$ and FF superconductivity, mentioned previously, assumes only one $\mathbf{Q}$ for which $\Delta_{\mathbf{Q}}$ (or equivalently, the $c_{N,\mathbf{Q}}$) is (are) nonzero, so $\Delta(\mathbf{r}) = \Delta_{\mathbf{Q}} e^{2i\mathbf{Q}\cdot\mathbf{r}}$. The time-reversal symmetric complement to the FF state has $\Delta(\mathbf{r}) = 2\Re\{\Delta_{\mathbf{Q}} e^{2i\mathbf{Q}\cdot\mathbf{r}}\}$ in which the real space fringes of $|\Delta(\mathbf{r})| = 2|\Delta_{\mathbf{Q}}|\cos(2\mathbf{Q}\cdot\mathbf{r}+\phi)$ are visible.

2.4 Quantum Monte Carlo

While having an analytic description of a physical system can be extremely valuable, it is often the case that a particular system may not lend itself to expression in some exact closed form. Furthermore, the approximations that may have been used to obtain said theory may not be completely valid to a given real physical system. In other cases, theories with exciting or novel predictions may require systems that are difficult to produce experimentally. In these cases, numerical simulations offer a relatively fast and low-cost method of either verifying the results of a theory or obtaining results for a system that defies analytic manipulation or experimental setup. In the case of spin-imbalanced fermion gases, some of the advantages of a numerical simulation are that the temperature of the system can be kept constant, even at absolute zero, and the fermion spins can be prevented from relaxing.

2.4.1 Pseudopotential

Any numerical simulation necessitates the introduction of certain simplifying approximations, similar to many analytic theories, and the approximations that are easy to deal with in theory are not always easy to implement in a simulation. For example, the BCS action introduced above uses the contact potential $V(\mathbf{x}) = -g\delta(\mathbf{x})$. However, this potential is difficult to model numerically, having infinite magnitude and gradient at the origin.

We therefore replace it with an ultratransferable pseudopotential (UTP) [41], a continuous, differentiable, piecewise defined polynomial of the same scattering length and effective range, ensuring equivalence of the scattering angle up to at least order k^2. This greatly eases the difficulty of modelling contact interactions numerically and allows us to work with continuous wavefunctions.

The explicit form of the UTP is

$$V(r) = \begin{cases} \left(1 - \dfrac{r}{L_\mathrm{c}}\right)^2 \left[u_1 \left(1 + \dfrac{2r}{L_\mathrm{c}}\right) + \displaystyle\sum_{i=2}^{N_\mathrm{u}} u_i \left(\dfrac{r}{L_\mathrm{c}}\right)^i\right], & r \leq L_\mathrm{c} \\ 0, & r > L_\mathrm{c} \end{cases}$$

where L_c is the cutoff length and $N_\mathrm{u} \geq 2$ is the number of optimizable parameters $\{u_i\}$. The optimization procedure to match the scattering phase shift was found to stop benefiting from an increase in the number of parameters at our choice of $N_\mathrm{u} = 3$. Except where the dependence on scattering length of the superconducting gap was under investigation, the scattering length was chosen to be such that the superconducting coherence length was less than the simulation cell size and the effective range was fixed at zero to match the contact potential.

The cutoff length L_c controls the extent of the potential in real space and is chosen to be equal to r_s, the average interparticle separation and the typical length scale above which a fermion could erroneously feel a potential from two other fermions simultaneously. The Fourier transform of the UTP at large k is oscillatory with amplitude decaying as $(L_\mathrm{c}k)^{-3/2}$, removing the ultraviolet divergence that would usually be present when using the contact potential.

This particular pseudopotential was chosen for its superlative accuracy compared to others over a wide range of parameter values, as detailed in [41]. It should be noted that specifying a scattering length and effective range are not enough to uniquely define a UTP; one also needs to set the units by specifying the fermion mass and the average fermion separation r_s.

2.4.2 Variational Monte Carlo

This project will make use of two Quantum Monte Carlo techniques, Variational Monte Carlo (VMC) and Diffusion Monte Carlo (DMC) [42]. In brief, Variational Monte Carlo involves varying the parameters of a trial wavefunction in order to minimize either the energy or the variance in energy, depending on the minimization scheme used. Close to the true wavefunction, the choice of scheme is unimportant as the

true ground state minimises both the energy and the variance [43] (the variance of the true ground state being zero) though in practice both methods are susceptible to being trapped in local minima that are not the global minimum, therefore care must be taken in inspecting the results to choose an appropriate minimisation scheme. VMC is thus the preferred method when dealing with any sort of optimization step.

Specifically, VMC evaluates expectation values of operators by taking samples in configuration space and calculating the value of 'local' operators. For example, the expectation value of the Hamiltonian H with respect to some wavefunction Ψ is

$$\langle H \rangle = \frac{\int \mathrm{d}\mathbf{R} E_{\mathrm{L}}(\mathbf{R}) |\Psi(\mathbf{R})|^2}{\int \mathrm{d}\mathbf{R} |\Psi(\mathbf{R})|^2}, \tag{2.30}$$

where $E_{\mathrm{L}}(\mathbf{R}) = \Psi^{-1}(\mathbf{R}) H \Psi(\mathbf{R})$ is the local energy and $\mathbf{R}$ is a $3N$-dimensional vector specifying the N-fermion configuration. This expectation value is evaluated by generating fermion configurations $\mathbf{R}$ according to the probability density $|\Psi(\mathbf{R})|^2$ (for a normalised Ψ) and finding the average of the local energy. The generation of these configurations is done in CASINO by making trial moves of single fermions and accepting or rejecting the moves in accordance with the Metropolis algorithm [44], where the Metropolis acceptance probability to accept a move from $\mathbf{R}'$ to $\mathbf{R}$ is

$$p(\mathbf{R}' \to \mathbf{R}) = \min\left(1, \frac{|\Psi(\mathbf{R})|^2}{|\Psi(\mathbf{R}')|^2}\right). \tag{2.31}$$

Provided detailed balance in configuration space is satisified, the resulting ensemble of configurations is distributed according to the aforementioned probability density [42], and from there it is a simple matter to determine the average of the local energies. The expectation values of other operators of interest, such as the momentum density or the condensate fraction, can likewise be easily calculated.

For spin-preserving interactions, the wavefunction used typically takes the Slater-Jastrow form, $\Psi = \mathrm{e}^{-J} D_\uparrow D_\downarrow$ where the D_σ are Slater determinants of single-particle wavefunctions of spin-species σ and J is the Jastrow factor which introduces additional correlations between fermions. This form of the wavefunction reproduces the Hartree-Fock wavefunction in the non-interacting limit where the single-particle wavefunctions are plane waves and the Jastrow factor is everywhere 0. The apparent lack of exchange antisymmetry between fermions of different spin is taken care of in the spin-part of the wavefunction, which does not appear as spin-preserving interactions do not operate on that space. If the wavefunction provided contains variational parameters, it is then possible to use VMC to optimise the wavefunction with respect to the variational parameters in order to obtain an estimate of both the ground state energy and the ground state wavefunction. Further details on the specifics of the CASINO implementation of sampling and optimisation in VMC can be found in the manual [37].

2.4.3 Diffusion Monte Carlo

DMC treats the Schrödinger equation as a diffusion equation in imaginary time and attempts to project out the ground state as the longest lived state on evolution, the decay rate of the amplitude of any

particular eigenstate contributing to the trial state being proportional to its energy [45]. This is done by generating a set of 'walkers', fermion configurations that are allowed to propagate via random walk to explore the phase space that are distributed according to the probability density given by the trial wavefunction. Theoretically, projection of the ground state should always be possible except where the trial wavefunction is perfectly orthogonal to the ground state, yet the DMC method is only exact in the limit of zero timestep and so in practice it is essential to first obtain a good trial wavefunction. It is for this reason that the use of DMC often involves first using VMC to optimise a variational trial wavefunction.

While more detailed information on the DMC method can be found elsewhere [37, 42, 46], a brief outline is as follows; Performing a Wick rotation to imaginary time [47], The Schrödinger equation becomes

$$-\frac{\partial}{\partial t}\Phi(\mathbf{R},t) = (H - E_{\text{ref}})\,\Phi(\mathbf{R},t) = \left(-\frac{1}{2}\nabla^2 + V(\mathbf{R}) - E_{\text{ref}}\right)\Phi(\mathbf{R},t), \tag{2.32}$$

where t is a real variable measuring the progress in imaginary time, E_{ref} is an (arbitrary) energy offset known as the reference energy and $\Phi(\mathbf{R},t)$ is the DMC wavefunction. Expanding in the Hamiltonian eigenfunction basis ϕ_i and looking at the infinite t limit, we obtain

$$\Phi(\mathbf{R},t) = \sum_i e^{-(E_i - E_{\text{ref}})t} c_i \phi_i(\mathbf{R}) \xrightarrow[t\to\infty]{} e^{-(E_0 - E_{\text{ref}})t} c_0 \phi_0(\mathbf{R}), \tag{2.33}$$

so the DMC wavefunction in this limit is proportional to the ground state wavefunction. It is for this reason that DMC is called a projector method.

If the potential part of the Hamiltonian H is neglected, the imaginary time Schrödinger equation takes the form of a diffusion equation while if the kinetic part is ignored, it becomes a rate equation. It is thus tempting to think of the initial state $\Phi(\mathbf{R},0)\sum_i c_i\phi_i(\mathbf{R})$ as a concentration or a probability distribution. However, for fermion systems, this interpretation is not possible as the wavefunction necessarily contains nodes. To fix this, one can introduce an importance sampling transformation [46] and consider the mixed distribution

$$f(\mathbf{R},t) = \Psi(\mathbf{R})\Phi(\mathbf{R},t), \tag{2.34}$$

which has the same sign everywhere if Ψ has the same nodal surface as Φ and obeys the modified Schrödinger equation

$$-\frac{\partial f}{\partial t} = -\frac{1}{2}\nabla^2 f + \nabla\cdot(\mathbf{v}f) + (E_{\text{L}} - E_{\text{ref}})f, \tag{2.35}$$

where $\mathbf{v}(\mathbf{R}) = \Psi^{-1}(\mathbf{R})\nabla\Psi(\mathbf{R})$ is the drift velocity and we see the re-emergence of the local energy operator. Compared to the equation for Φ alone, the only difference is a modification of the ordinary spatially varying potential to a velocity dependent one, that is the addition of a drift process. The

sign problem has thus been solved with no major additional complication to the interpretation of the governing equation of f as being composed of drift-diffusive and rate processes.

In the limit of small time slices, that is small time steps, the kinetic and potential operators approximately commute, the commutator being proportional to the timestep, and so it is possible to decouple the diffusion and rate processes. The diffusion process is modelled by the movement of walkers, fermion configurations $\mathbf{R}$ that propagate via random walk and the rate process is modelled by the 'branching' of configurations. Branching involves the replicating or deleting of walkers at appropriate rates so that their population and spread in configuration space continues to reflect the probability distribution given by the wavefunction. This decoupling of processes is expressed mathematically as a decomposition of the Green's function governing the evolution of f as

$$G(\mathbf{R}' \to \mathbf{R}, \tau) \xrightarrow[\tau \to 0^+]{} G_{\mathrm{D}}(\mathbf{R}' \to \mathbf{R}, \tau) G_{\mathrm{B}}(\mathbf{R}' \to \mathbf{R}, \tau), \tag{2.36}$$

where τ is the timestep,

$$G_{\mathrm{D}}(\mathbf{R}' \to \mathbf{R}, \tau) = \frac{1}{(2\pi\tau)^{3N/2}} \exp\left(-\frac{1}{2\tau}(\mathbf{R} - \mathbf{R}' - \tau \mathbf{v}(\mathbf{R}'))^2\right), \tag{2.37}$$

is the drift-diffusion Green's function and

$$G_{\mathrm{B}}(\mathbf{R}' \to \mathbf{R}, \tau) = \exp\left(-\frac{\tau}{2}(E_{\mathrm{L}}(\mathbf{R}) + E_{\mathrm{L}}(\mathbf{R}') - 2E_{\mathrm{ref}})\right), \tag{2.38}$$

is the branching factor. As this decomposition is only exact in the limit of zero timestep, it is customary to extrapolate results to zero timestep.

The CASINO implementation of DMC works by taking a trial wavefunction that has been optimised in VMC as Ψ (implicitly assuming that the optimised wavefunction has the correct nodal surface), generating configurations using VMC and using those for DMC equilibration, where the random walk through configuration space of the walkers is governed by G_{D} and their population controlled by G_{B}, with the reference energy E_{ref} varied to keep the total number of walkers at a preset amount. Expectation values can then be calculated on the equilibrium walker population. For example, the energy is calculated as

$$E_{\mathrm{DMC}} \equiv E_0 = \frac{\int \mathrm{d}\mathbf{R} f(\mathbf{R}, t \to \infty) E_{\mathrm{L}}(\mathbf{R})}{\int \mathrm{d}\mathbf{R} f(\mathbf{R}, t \to \infty)}. \tag{2.39}$$

2.4.4 Heavy-tailed statistics

In any Monte Carlo study it is necessary to understand the underlying distribution of the observables which the Monte Carlo procedure attempts to estimate in order to ensure correctness of the statistical treatment of errors. As previously mentioned, many-fermion trial wavefunctions necessarily contain nodes and importance sampling guided by these trial wavefunctions leads to divergences in locally

sampled quantities such as the energy [48]. For this project, we will primarily be interested in the energy, condensate fraction and momentum density.

Heuristically, near a nodal surface the N-fermion trial wavefunction, Ψ_{T}, varies at least linearly with the separation from the nodal surface, x, $\Psi_{\mathrm{T}}(x) \sim x$, and so the probability distribution used for importance sampling varies as at least the square of x, $P(x) \equiv |\Psi_{\mathrm{T}}(x)|^2 \sim x^2$. For a given Hamiltonian H, $H\Psi_{\mathrm{T}}(x)$ will then take some value that is generically not zero unless Ψ_{T} is the true ground state wavefunction. The local energy E_{L} thus varies inversely with x near a nodal surface, $E_{\mathrm{L}}(x) \equiv \Psi_{\mathrm{T}}^{-1}(x) H \Psi_{\mathrm{T}}(x) \sim 1/x$, leading to an energy distribution near the nodal surfaces of the form $P(E_{\mathrm{L}}) = \int_S \frac{P(\mathbf{R})}{|\nabla_{\mathbf{R}} E_{\mathrm{L}}|} \mathrm{d}^{3N-1}\mathbf{R} \sim x^4 \sim E_{\mathrm{L}}^{-4}$ where the integration is over the $3N-1$ dimensional constant energy surface S near the nodal surface. As the $3N-1$ dimensions being integrated over are orthogonal to the nodal separation variable x, they do not contribute to powers of x near the nodal surface, leading to the inverse fourth power distribution of the local energy shown above. This distribution is leptokurtotic, having heavier tails and thus a greater proportion of outliers when compared to the Gaussian distribution.

This derived form of the distribution is valid near the nodal surface, that is for small x or equivalently large $|E_{\mathrm{L}}|$, so the power law describes the tails of the distribution. Any observable O with local operator varying near the nodal surface as $O_{\mathrm{L}} \sim 1/x^n$ will have a probability distribution $P(O_{\mathrm{L}}) \sim O_{\mathrm{L}}^{-(1+3/n)}$; for example, the condensate fraction c, being a two-particle correlator, varies as $1/x^2$ near the nodal surface and so has the tails of the probability distribution varying as $P(c) \sim c^{-5/2}$ while the momentum density n_k has the same distribution as the energy, $P(n_k) \sim n_k^{-4}$.

It bears mentioning that for $n \geq 3/2$, the second moment of the distribution no longer exists, invalidating the use of the Central Limit Theorem [49]. For example, as with the condensate fraction above, the variance of the energy varies as $V_E \sim 1/x^2$ leading to a probability distribution of $P(V_E) \sim V_E^{-5/2}$, which has an undefined second moment and thus the average of samples of the variance does not have a Gaussian distribution. However, the second moment of the local energy ditribution does exist, and so in the limit of many samples, the average of the local energy converges to a Gaussian distribution. As such, the sample energy obtained from VMC or DMC is a good estimator of the true energy provided many samples are taken, but the sample variance of the energy is generically not a measure of the error. While this presents a significant theoretical problem regarding the interpretation of the sample variance of such quantities, in practice it was found that the weight in the tails is small enough that major outliers are unlikely to appear even within 10^7 samples. Thus, the issue of heavy-tailed statistics will be temporarily postponed and the sample variance quoted in lieu of an error measure. Future work is planned to rectify this.

As a final remark, it has been shown that the issue of heavy tails can be remedied through an appropriate choice of sampling strategy [50], however this greatly increases the computational burden, fully halving the computation speed and so will not be used in the present study.

Chapter 3

Communal pairing theory

Having covered the relevant background, we are now well-positioned to begin extending FFLO theory. This will be done by relaxing the exclusive pairing condition, which stipulates that any one fermion state is tied to one and only one other, regardless of the quantum numbers (spin, momentum, band) used to identify the particular states. By relaxing this condition, it is now possible to consider states as being shared between different pairs and this “communal pairing" analysis claims to result in a state that is lower in energy than the comparable FFLO state.

For clarity, we state that we are not positing bound states of more than 2 fermions, only additional superconducting correlations with a range of pair momenta. This may be thought of as any particular fermion being only weakly bound with its pair complement and ready to bind with other fermions of the same spin but different momentum.

This chapter is a modified and streamlined version of a paper published in Europhysics Letters in 2019 [1]. My PhD supervisor Dr. Gareth Conduit provided useful input and helped edit the paper. The analytic work was split between Dr. Thomas Whitehead and myself.

It has been shown in a few-fermion context [36] that an instability containing more majority than minority-spin fermions maximizes the binding energy captured in spin-imbalanced systems by taking advantage of the correlations between all available momentum states. Such an instability involves non-exclusive pairing between several majority-spin fermions and one minority-spin fermion in an ensemble called a communal state. An example state is shown in Fig. 3.1, with three majority- (up-)spin fermions each paired (having nontrivial superconducting correlations) with the same minority- (down-)spin fermion. This inspires us to merge Cooper pairs that share a minority-spin fermion to construct a communal superconducting state that correlates all available momentum states on the Fermi surfaces.

To explore communal superconductivity we examine a two-spin fermionic system with an attractive contact interaction. The quantum partition function, $\mathscr{Z} = \int \mathscr{D}(\psi, \bar{\psi}) \mathrm{e}^{-S[\psi,\bar{\psi}]}$, depends upon the BCS action

$$S[\psi,\bar{\psi}] = \sum_{\omega,\mathbf{k},\sigma} \bar{\psi}_{\mathbf{k},\sigma}(-i\omega + \xi_{\mathbf{k},\sigma})\psi_{\mathbf{k},\sigma} - g \sum_{\omega,\mathbf{k},\mathbf{k}',\mathbf{q}} \bar{\psi}_{\mathbf{k}+\frac{\mathbf{q}}{2},\uparrow} \bar{\psi}_{-\mathbf{k}+\frac{\mathbf{q}}{2},\downarrow} \psi_{-\mathbf{k}'+\frac{\mathbf{q}}{2},\downarrow} \psi_{\mathbf{k}'+\frac{\mathbf{q}}{2},\uparrow}, \tag{3.1}$$

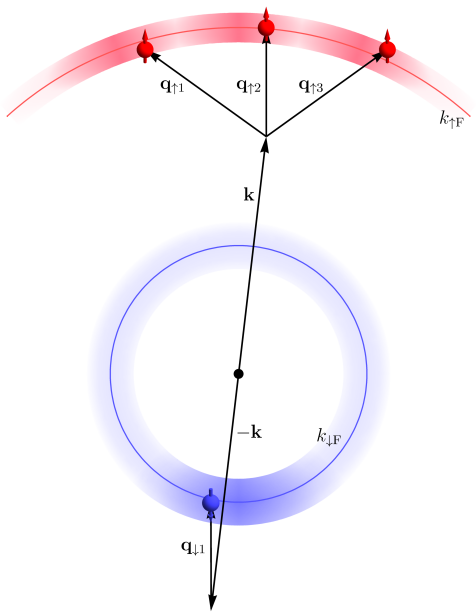

Fig. 3.1 Idealized representation of the spin-imbalanced system showing Fermi surfaces for the down- (light blue circle) and up-spin (light red arc) species, with occupiable momentum states extending over a momentum scale set by the Debye frequency, forming annuli. The intensity of color in the annuli indicate the approximate extent of the superconducting correlations. Also shown are the momenta of $(N_\uparrow, N_\downarrow) = (3,1)$ up- and down-spin fermions with corresponding q-vectors $\mathbf{q}_{\sigma i}$. The angular spread of the up-spin fermion momenta is exaggerated for clarity.

where $\psi_{\mathbf{k},\sigma}$ and $\bar{\psi}_{\mathbf{k},\sigma}$ are a fermion field and its Grassmann conjugate, for momentum $\mathbf{k}$ and spin species $\sigma \in \{\uparrow,\downarrow\}$, $\xi_{\mathbf{k},\sigma}$ is the species-dependent dispersion, $g > 0$ is the strength of the attractive contact interaction, and ω is a fermionic Matsubara frequency. In this expression the momenta $\mathbf{q}$, referred to henceforth as q-vectors, give the net momenta of coupled fermions. Our strategy is to build on the original BCS and FFLO theories that are directly applicable to the solid state, and sohere adopt a Debye frequency cutoff on the sums over $\mathbf{k}$, however similar results are obtained in cold atom gases provided proper regularization is carried out.

We perform a Hubbard-Stratonovich decoupling in the Cooper channel, using a concise matrix formalism to express the action as

$$S[\psi,\Delta] = \sum_{\omega,\mathbf{k}} \begin{pmatrix} \bar{\boldsymbol{\psi}}_\uparrow \\ \boldsymbol{\psi}_\downarrow \end{pmatrix}^{\mathrm{T}} \begin{pmatrix} \mathscr{G}_\uparrow^{-1} & -\boldsymbol{\Delta} \\ -\boldsymbol{\Delta}^\dagger & \mathscr{G}_\downarrow^{-1} \end{pmatrix} \begin{pmatrix} \boldsymbol{\psi}_\uparrow \\ \bar{\boldsymbol{\psi}}_\downarrow \end{pmatrix} + \sum_\omega \frac{\mathrm{Tr}(\boldsymbol{\Delta}^\dagger \boldsymbol{\Delta})}{g}, \tag{3.2}$$

where the vectors $\boldsymbol{\psi}_\sigma = (\psi_{(\mathbf{q}_{\sigma 1}+\varsigma_\sigma \mathbf{k}),\sigma}, \psi_{(\mathbf{q}_{\sigma 2}+\varsigma_\sigma \mathbf{k}),\sigma}, \ldots)^{\mathrm{T}}$, with $\varsigma_\uparrow = +1$ and $\varsigma_\downarrow = -1$, the Grassman conjugates $\bar{\boldsymbol{\psi}}_\sigma$ are similar, the matrices $\mathscr{G}_\sigma^{-1} = \mathrm{diag}(\mathscr{G}^{-1}_{(\mathbf{q}_{\sigma 1}+\varsigma_\sigma \mathbf{k}),\sigma}, \mathscr{G}^{-1}_{(\mathbf{q}_{\sigma 2}+\varsigma_\sigma \mathbf{k}),\sigma}, \ldots)$, for $\mathscr{G}^{-1}_{\mathbf{p},\sigma} = -i\omega + \varsigma_\sigma \xi_{\mathbf{p},\sigma}$, and

$$\boldsymbol{\Delta} = \begin{pmatrix} \Delta_{\mathbf{q}_{\uparrow 1}+\mathbf{q}_{\downarrow 1}} & \Delta_{\mathbf{q}_{\uparrow 1}+\mathbf{q}_{\downarrow 2}} & \cdots \\ \Delta_{\mathbf{q}_{\uparrow 2}+\mathbf{q}_{\downarrow 1}} & \Delta_{\mathbf{q}_{\uparrow 2}+\mathbf{q}_{\downarrow 2}} & \cdots \\ \vdots & \vdots & \ddots \end{pmatrix},$$

where the $\mathbf{q}_{\sigma i}$ run over all the q-vectors of species σ. We label the number of fermions in the underlying instability, and hence the number of q-vectors, per species by N_σ: therefore the $\mathscr{G}_\sigma^{-1}$ are $N_\sigma \times N_\sigma$ matrices and $\boldsymbol{\Delta}$ is an $N_\downarrow \times N_\uparrow$ matrix. We shall find that in spin-imbalanced systems $N_\uparrow \neq N_\downarrow$, so that

$\mathbf{\Delta}$ is rectangular rather than square, and different numbers of fermions from each species are involved in the underlying instability. In the system represented by Fig. 3.1, where there are three up-spin and one down-spin fermions involved in the underlying instability, $\mathbf{\Delta}$ would be a 1×3 matrix. We focus our analysis on the Cooper channel as recent work [51] shows that in the BCS limit, screening [19] and pairing mechanisms decouple so the reduction in critical temperature due to particle-hole interactions for both our communal state and for FFLO will be the same. We note for completeness that decoupling through the magnetic channel was also considered but had no consequence.

The elements of the $\mathbf{\Delta}$ matrix gap the dispersion. For the Fulde–Ferrell (FF) state (also referred to as single-plane-wave superconductivity in the literature) $\mathbf{\Delta}$ has only a single entry, and for crystalline FFLO superconductivity [52, 22] it is diagonal. The non-diagonal form here allows communal superconductivity, as in common with the few-fermion analysis [36] multiple majority-spin fermions share a minority-spin fermion. We focus on superconductivity where the sharing majority-spin fermions have nearly aligned q-vectors, comparable to the FF state. For simplicity of analysis we assume that none of the $\mathbf{q}_{\uparrow i}+\mathbf{q}_{\downarrow j}$ pairs of q-vectors in $\mathbf{\Delta}$ are degenerate. Following Ref. [36] the $\mathbf{q}_{\sigma i}$ vectors are taken to be not equal to each other so that each $\psi_{\mathbf{p},\sigma}$ appears only once in Eq. (3.2). This corresponds to assigning states on the Fermi surfaces into non-overlapping communal states of equal angular width.

With this expression for the action, working in the mean-field approximation we can carry out a Ginzburg-Landau expansion of the regularized thermodynamic potential to obtain

$$\Omega = T\sum_{\omega,\mathbf{k}}\sum_{n=1}^{\infty}\frac{1}{n}\mathrm{Tr}\left(\mathscr{G}_{\uparrow}\mathbf{\Delta}\mathscr{G}_{\downarrow}\mathbf{\Delta}^{\dagger}\right)^{n}+\frac{\mathrm{Tr}\left(\mathbf{\Delta}^{\dagger}\mathbf{\Delta}\right)}{g}, \tag{3.3}$$

where T is the temperature. To make progress with this expression, we symmetrize the coupling amplitudes, $\Delta_{\mathbf{q}}=\Delta$. Near the second-order transition to the normal state we may neglect the effect of high-order terms in Δ, allowing us to truncate the expression for the thermodynamic potential to

$$\Omega = \alpha\Delta^{2}+\frac{1}{2}\beta\Delta^{4}+\ldots, \tag{3.4}$$

where

$$\begin{aligned}\alpha &= \sum_{\mathbf{q}_{\uparrow},\mathbf{q}_{\downarrow}}\left(\frac{1}{g}+T\sum_{\omega,\mathbf{k}}\mathscr{G}_{\mathbf{q}_{\uparrow}+\mathbf{k},\uparrow}\mathscr{G}_{\mathbf{q}_{\downarrow}-\mathbf{k},\downarrow}\right),\\ \beta &= T\sum_{\substack{\mathbf{q}_{\uparrow 1},\mathbf{q}_{\downarrow 1},\\ \mathbf{q}_{\uparrow 2}\,\mathbf{q}_{\downarrow 2}}}\sum_{\omega,\mathbf{k}}\mathscr{G}_{\mathbf{q}_{\uparrow 1}+\mathbf{k},\uparrow}\mathscr{G}_{\mathbf{q}_{\downarrow 1}-\mathbf{k},\downarrow}\mathscr{G}_{\mathbf{q}_{\uparrow 2}+\mathbf{k},\uparrow}\mathscr{G}_{\mathbf{q}_{\downarrow 2}-\mathbf{k},\downarrow}.\end{aligned} \tag{3.5}$$

To evaluate these expressions, we specialize to the case of small Debye frequency, found for many conventional superconductors [53–55]. In this limit, the vectors $\mathbf{q}_{\sigma i}$ are expected to be approximately parallel to maximise the number of contributing occupiable momentum states. Approximately parallel but unequal $\mathbf{q}_{\sigma i}$ vectors provide a natural tiling of the Fermi surfaces into non-overlapping communal

states. This enables us to factorize out combinatorial factors, giving

$$\begin{aligned}\alpha &= N_\uparrow N_\downarrow \left(\frac{1}{g} + T\sum_{\omega,\mathbf{k}} \mathscr{G}_{\mathbf{q}+\mathbf{k},\uparrow}\mathscr{G}_{\mathbf{q}-\mathbf{k},\downarrow}\right), \\ \beta &= N_\uparrow N_\downarrow \left[J_0 + (N_\uparrow - 1)J_\uparrow + (N_\downarrow - 1)J_\downarrow + (N_\uparrow - 1)(N_\downarrow - 1)J_{\uparrow\downarrow}\right],\end{aligned} \tag{3.6}$$

where $J_0 = J(\mathbf{q},\mathbf{q},\mathbf{q},\mathbf{q})$, $J_\uparrow = J(\mathbf{q}+\delta\mathbf{q}_\uparrow,\mathbf{q},\mathbf{q}-\delta\mathbf{q}_\uparrow,\mathbf{q})$, $J_\downarrow = J(\mathbf{q},\mathbf{q}+\delta\mathbf{q}_\downarrow,\mathbf{q},\mathbf{q}-\delta\mathbf{q}_\downarrow)$, and $J_{\uparrow\downarrow} = J(\mathbf{q}+\delta\mathbf{q}_\uparrow,\mathbf{q}+\delta\mathbf{q}_\downarrow,\mathbf{q}-\delta\mathbf{q}_\uparrow,\mathbf{q}-\delta\mathbf{q}_\downarrow)$. Here $\mathbf{q}$ is taken to represent the average q-vector for the fermions, symmetrized between species, and $\delta\mathbf{q}_\sigma$ is half the average separation between q-vectors for species σ, which in the small Debye frequency limit is orthogonal to the vector $\mathbf{q}$. We follow the prescription of Ref. [36] that the angular widths of the regions of Fermi surface involved in the communal superconducting state are the same between species, so the arc lengths $\delta\mathbf{q}_\sigma$ are proportional to the Fermi momenta and $|\delta\mathbf{q}_\uparrow|/|\delta\mathbf{q}_\downarrow| = k_{\mathrm{F},\uparrow}/k_{\mathrm{F},\downarrow}$, where $k_{\mathrm{F},\sigma}$ is the Fermi momentum of species σ. Following the method of Ref. [52], for a free dispersion the function $J(\mathbf{q}_1,\mathbf{q}_2,\mathbf{q}_3,\mathbf{q}_4)$ may be evaluated at zero temperature as

$$\begin{aligned}J(\mathbf{q}_1,\mathbf{q}_2,\mathbf{q}_3,\mathbf{q}_4) &= T\sum_{\omega,\mathbf{k}} \mathscr{G}_{\mathbf{q}_1+\mathbf{k},\uparrow}\mathscr{G}_{\mathbf{q}_2-\mathbf{k},\downarrow}\mathscr{G}_{\mathbf{q}_3+\mathbf{k},\uparrow}\mathscr{G}_{\mathbf{q}_4-\mathbf{k},\downarrow} \\ &= \frac{\mathscr{N}}{4\delta\mu^2}\mathrm{Re}\int_0^1 \frac{(-1)^D \mathrm{d}x\mathrm{d}y}{\left[1-\left(\frac{|\mathbf{q}_1(x-1)+\mathbf{q}_2(y-x)-\mathbf{q}_3 y|k_\mathrm{F}}{\delta\mu}\right)^2\right]^{3/D}},\end{aligned} \tag{3.7}$$

where $\mathscr{N} = \frac{mL^2}{\pi}$ is the density of states in energy with L the linear system size, $\delta\mu = (k_{\mathrm{F},\uparrow}^2 - k_{\mathrm{F},\downarrow}^2)/4$ is the chemical potential difference between the species, $k_\mathrm{F} = (k_{\mathrm{F},\uparrow} + k_{\mathrm{F},\downarrow})/2$ is the average Fermi momentum, and $D \in \{2,3\}$ is the dimensionality. Eq. (3.7) confirms that for a single instability $\beta \geq 0$ for realistic values of the $\mathbf{q}_i$ [22], justifying the truncation in Eq. (3.4).

To identify the optimal ratio of number of fermions involved in the communal superconductor, we express Eq. (3.4) as a function of $N_\uparrow/N_\downarrow$ and $N_\uparrow N_\downarrow$, and then optimize Ω with respect to $N_\uparrow/N_\downarrow$, $N_\uparrow N_\downarrow$, and Δ simultaneously. This gives the expected ratio of number of fermions involved in the underlying instability as

$$\frac{N_\uparrow}{N_\downarrow} = \frac{J_{\uparrow\downarrow} - J_\downarrow}{J_{\uparrow\downarrow} - J_\uparrow} = \left(\frac{|\delta\mathbf{q}_\uparrow|}{|\delta\mathbf{q}_\downarrow|}\right)^2 = \left(\frac{\nu_\uparrow}{\nu_\downarrow}\right)^{2/(D-1)}, \tag{3.8}$$

where the second equality was obtained from Eq. (3.7), ν_σ is the density of states in momentum at the Fermi surface of species σ.

This result confirms that the superconducting state is indeed communal, with pairs sharing minority-spin fermions to take advantage of all available correlations in spin-imbalanced systems. Eq. (3.8) also aligns with our heuristic expectation that the instability involves more fermions of the species with the larger density of states in momentum at its Fermi surface, as was also found in the few-fermion case [36]. For spin-balanced systems, $\nu_\uparrow = \nu_\downarrow$ and so $N_\uparrow/N_\downarrow = 1$, recovering the BCS theory result, whilst in the polaron limit of a single minority-spin impurity in a full Fermi sea of majority-spin fermions, the single minority-spin fermion couples with all the majority-spin fermions at their Fermi surface, in agreement

with results from the literature [56–58]. FFLO superconductivity is predicted in one dimension, as there $\nu_\uparrow = \nu_\downarrow$ regardless of the spin-imbalance.

The same optimization procedure that gave Eq. (3.8) for the ratio $N_\uparrow/N_\downarrow$ also provides an expression for the product $N_\uparrow N_\downarrow$, as

$$N_\uparrow N_\downarrow = \frac{\left(J_0 - J_\uparrow - J_\downarrow + J_{\uparrow\downarrow}\right)^2}{\left(J_{\uparrow\downarrow} - J_\uparrow\right)\left(J_{\uparrow\downarrow} - J_\downarrow\right)}. \tag{3.9}$$

For reasonable values of the $|\delta\mathbf{q}_\sigma|$ and $|\mathbf{q}|$ in spin-imbalanced systems this expression gives values of $N_\uparrow N_\downarrow > 1$, confirming that the communal superconductor is indeed made up of multiple fermions of at least one spin species. Excessively high $N_\uparrow N_\downarrow$ is energetically penalized by the highest term in the expansion of the thermodynamic potential, which goes as $(N_\uparrow N_\downarrow \Delta^2)^n$, and so we expect communal superconductivity to have both N_σ being reasonably small integers. In the spin-balanced limit Eq. (3.9) collapses to the BCS result $N_\uparrow N_\downarrow = 1$.

Although the discussion above focuses on nearly aligned q-vectors, comparable to the FF state, it is known that the Larkin–Ovchinnikov state [8] built from two plane-waves can be energetically favorable to single-plane-wave superconductivity. Therefore, we now follow the prescription of Larkin and Ovchinnikov and construct a communal superconducting state out of two instabilities on opposite sides of the Fermi surfaces. The only differences in the theory of communal superconductivity for one and two instabilities are a multiplicative factor of 2 in Eq. (3.4) and additional terms in the expression for β in Eq. (3.6). Similarly to the single instability case the optimal instability contains more up- than down-spin fermions, and so the communal superconducting state is also energetically favorable over the Larkin–Ovchinnikov state.

Chapter 4

Quantum Monte Carlo

Having laid the qualitative motivation and analytic foundation for communal pairing, we move on now to its numerical verification. The results presented in this chapter are a combination of those published in 2 papers, one in Europhysics Letters [1] and one in Physical Review A [2], both in 2019. The work presented here is my own, with Dr. Conduit providing assistance with the Quantum Monte Carlo software and editing the papers.

4.1 Method

As mentioned previously, numerical simulations are valuable in situations for which strict and exact analytic treatment is difficult, contentious or impossible, and for which the construction of materials or other physical systems that exhibit the desired effects is problematic or costly. 2DFGs fulfill these conditions, particularly in the case where the spin-imbalance is large enough that a visible difference is expected between FFLO and communal superconducting phases. It is for this reason that we make use of Quantum Monte Carlo to obtain complementary evidence as to the correctness of these theories.

4.1.1 Overview

We make use of the CASINO program to simulate spin-imbalanced fermion gases. Low dimensionality is known to enhance quantum effects and furthermore brings practical benefits in that the number of particles and thus the simulation time is reduced. Therefore, we elect to focus on 2D systems, as that is the lowest dimension at which FFLO and communal superconductivity mentioned in the preceding chapter can be distinguished.

A base case system is set up as follows: first, a simulation cell geometry is selected and the desired number of up and down spin fermions is chosen. The simulation cell area is then calculated and an ultratransferable pseudopotential generated such that the coherence length is equal to the linear dimension of the simulation area. A trial wavefunction suitable for the selected number of fermions is generated with variational parameters as appropriate and optimised under the given interaction pseudopotential.

Histograms of the obtained energy values revealed that the effect of the heavy tailed distributions were not obvious up to 10^7 samples and so the effect of the heavy tails is neglected for the present and the sample error assumed to be a good estimate of the true statistical error.

Once a sufficiently optimised wavefunction is obtained, it is then used as the basis for DMC where the parameters of interest are the energy, the momentum density of the two spin-species and the condensate fraction in momentum space [59]. The energy is gathered by default in CASINO and is generally useful to track the progress of optimisation and to quantify the additional accuracy obtained by doing DMC over VMC. The momentum density is collected to give insight into the type of many-particle state formed; for example, very different momentum densities are expected for the FFLO state, breached superfluids [28, 29] and systems that have exceeded the Chandrasekhar-Clogston limit [32–35]. However, it is not possible to distinguish between FFLO and communal superconductivity from the momentum density alone and indeed the momentum density does not constitute a direct measurement of superconductivity. Thus, we also calculate the condensate fraction in momentum space, which is estimated from the two body density matrix and is approximately equal to the modulus squared of the superconducting gap parameter.

This cycle of setup–optimisation–data gathering is then repeated for a variety of parameters, some with clear physical significance, such as the scattering length and spin-imbalance, and others that are more simulation parameters, such as the DMC timestep and the cutoff length of the UTP.

4.1.2 Trial wavefunction

We follow after previous work [60] and employ a Slater-Jastrow trial wavefunction of the form

$$\Psi_{\mathrm{T}} = \mathrm{e}^{-J} \det[\phi(\mathbf{s}_{i,j})],$$

The determinant ensures the correct fermionic spin-symmetry. The pairing orbital $\phi(\mathbf{s}_{i,j})$ is given by

$$\phi(\mathbf{s}_{i,j}) = \sum_{l=1}^{n_{\mathrm{p}}} \cos(\mathbf{k}_l \cdot \mathbf{s}_{i,j}) + \Theta_{\mathbb{Z}}(N_\downarrow - i) \left(1 - \frac{s_{i,j}}{L_{\mathrm{p}}}\right)^3 \Theta_{\mathbb{R}} \left(1 - \frac{s_{i,j}}{L_{\mathrm{p}}}\right) \sum_{m=0}^{n_{\mathrm{r}}} a_m s_{i,j}^m,$$

where $\mathbf{s_{i,j}} \equiv \mathbf{r}_{\uparrow,\mathbf{i}} - \Theta_{\mathbb{Z}}(N_\downarrow - i)\mathbf{r}_{\downarrow,\mathbf{j}}$, $s_{i,j} \equiv \left|\mathbf{s_{i,j}}\right|$, $\Theta_{\mathbb{Z}}$ is the discrete Heaviside step function defined as zero for negative integer arguments and one for non-negative integer arguments, $\Theta_{\mathbb{R}}$ the continuous Heaviside step function, $\mathbf{k}_l$ the l^{th} shortest reciprocal-space vector of the simulation cell, n_{p} and n_{r} the expansion order of the plane wave and polynomial parts of the wavefunction, L_{p} the cutoff length of the polynomial wavefunction, $\{p_l\}$ the plane wave coefficents, $\{a_m\}$ the set of optimisable polynomial coefficients, and $N_\downarrow$ the number of down-spin fermions. As before, we have assumed, without loss of generality, that the down-spin fermions are the minority species.

The value of n_{p} is set by the lattice geometry and the number of fermions in the system so that the highest $\mathbf{k}_l$ appearing in the wavefunction is the highest momentum state of the non-interacting system.

The cosine part of the pairing wavefunction equals the ground state wavefunction for the non-interacting fermion gas. This near equivalence is reflective of considering only weakly interacting fermion gases.

In the presence of attractive interactions, the polynomial component of the pairing orbital can shift the nodal surface to smoothly transform to a superconducting wavefunction. The polynomial cutoff L_p is chosen such that this part of the wavefunction extends into the corners of the simulation cell. The cubic cutoff ensures continuity of the local energy. $n_\mathrm{r} = 2$ was chosen as the incremental gain in decrease of variational energy from increasing n_r further was less than the statistical error.

To capture additional fermion correlations, we include the Jastrow factor J

$$J = \sum_{i,j,k} u_k r_{i,j}^{k-1} \left(1 - \frac{r_{i,j}}{r_s}\right)^3 \Theta\left(1 - \frac{r_{i,j}}{r_s}\right) + \nu \text{ terms}$$

where $r_{i,j} \equiv |\mathbf{r}_{\uparrow,i} - \mathbf{r}_{\downarrow,j}|$,, and the $\{u_k\}, \{p_m\}$ are optimisable parameters. J is a function of all opposite-spin fermion separations containing a short range isotropic u term and a ν term [61] that reflects the simulation cell symmetry and whose form is omitted for brevity. An anisotropic term was considered for the Jastrow factor but it was found that its coefficients on minimising the energy were zero and so the term was omitted.

The wavefunction is optimised using VMC before a separate VMC run generates a population of walkers for DMC, which are allowed to equilibrate before expectation values are calculated. Both VMC and DMC simulations are done in the zero temperature limit and so we ignore such effects as spin-relaxation.

4.1.3 Expectation values

The expectation values that are of concern here are the energy, the momentum density and the condensate fraction. Calculation of the energy is relatively straightforward and has been detailed in subsections 2.4.2 and 2.4.3. The momentum density and condensate fraction are explicitly calculated in momentum space, rather than being determined indirectly as the fourier transform of the same quantities in real space. This is done as the Fourier transforms neglect the simulation cell corners and so bias the result at small momenta [59].

Momentum density The momentum density is the fourier transform of the one-body density matrix and is defined as $n_{\mathbf{k},\sigma} \equiv \langle c^\dagger_{\mathbf{k},\sigma} c_{\mathbf{k},\sigma} \rangle$. For the BCS wavefunction of Eq. 2.21, this evaluates to $n_{\mathbf{k},\sigma} = |v_\mathbf{k}|^2$, where we have used $|v_\mathbf{k}|^2 = |v_{-\mathbf{k}}|^2$.

Condensate fraction The condensate fraction estimator used in CASINO is a modified form of the two-body density matrix and is defined explicitly as $c_\mathbf{q} \equiv \sum_\mathbf{k} \left(\langle c^\dagger_{\mathbf{k},\uparrow} c^\dagger_{\mathbf{q}-\mathbf{k},\downarrow} c_{\mathbf{q}-\mathbf{k},\downarrow} c_{\mathbf{k},\uparrow} \rangle - n_{\mathbf{k},\uparrow} n_{\mathbf{q}-\mathbf{k},\downarrow} \right)$. It therefore is the difference between the two-body density matrix and a product of one-body density matrices. This is done to ensure that only two-body effects are captured. For the BCS wavefunction, it evaluates to $c_\mathbf{q} = \delta_{\mathbf{q},\mathbf{0}} \sum_\mathbf{k} |u_\mathbf{k}|^2 |v_\mathbf{k}|^2 = \delta_{\mathbf{q},\mathbf{0}} \frac{|\Delta|}{8\pi} (\tan^{-1} \frac{\mu}{|\Delta|} + \frac{\pi}{2}) \to \delta_{\mathbf{q},\mathbf{0}} \frac{|\Delta|}{8}$ for $\mu \gg |\Delta|$. The condensate

fraction is therefore an estimate of $|\Delta|$. We use the condensate fraction rather than calculate the gap directly as the CASINO code cannot evaluate expectation values of objects that do not preserve particle number.

4.1.4 Simulation setup and convergence

With the simulation methodology in place the final step is to set up the system. The major considerations are the size and shape of the simulation cell that could lead to finite size errors.

We employed two forms of simulation cell; a rhomboidal and square box, giving triangular and square tilings respectively in momentum space. Both geometries gave quantitatively similar results. A triangular lattice has the densest possible tiling of momentum points in 2D, giving the closest to circular Fermi surfaces and thereby minimizing finite size effects [62, 63]. This was confirmed by varying the number of particles simulated in our DMC studies varied from 26 to 164, which compares favourably with DMC studies conducted on other systems [64, 65]. Finally, in the non-interacting and balanced system limits the results obtained compared favourably to known analytical results in the thermodynamic limit. Therefore, in these paradigmatic systems our simulations were free of finite size effects.

4.2 Results

4.2.1 Spin-balanced BCS state

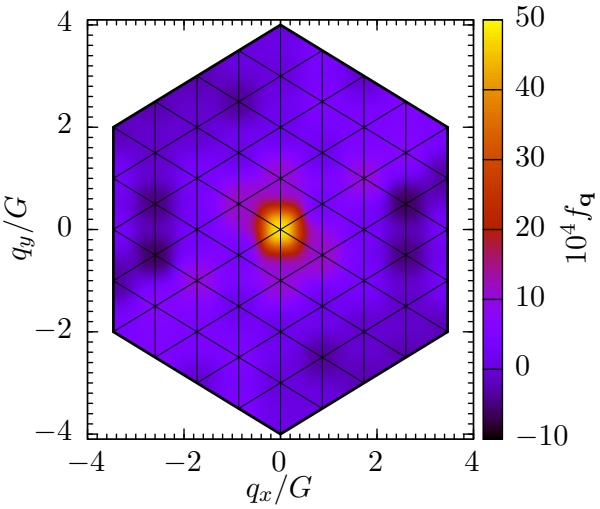

Fig. 4.1 Plot of the condensate fraction in pair-momentum space for the spin-balanced case with 37 fermions of each species. The wavevectors are scaled in units of the reciprocal lattice vector G and black lines denote the q-space grid. A BCS type condensate peak is clearly visible at $q = 0$, entirely contained within a single lattice spacing. Everywhere else the condensate fraction is observed to slightly fluctuate about 0.

We start from the well-established spin-balanced BCS system to confirm the accuracy of our simulations, and later explore imbalance. To build our investigation from a solid platform, we first study a spin-balanced system with 37 spin up and spin down fermions. We select a scattering length $a = 5.6r_s$ and effective range $r_e = 0$ to ensure that the superconducting coherence length is less than the size of the simulation cell.

The accumulated condensate fraction is shown in Fig. 4.1. The condensate fraction at $q = 0$ was 8 sample standard deviations above zero while those at every other q point were within 2 sample standard deviations of zero. The reduction in energy of the interacting system compared to the non-interacting system meanwhile agrees with that obtained from analytic calculation [40, 38]. The results obtained for the spin-balanced case are therefore in line with theoretical expectations of BCS theory [4] and we proceed with confidence in the veracity of the simulations.

We note for completeness that the condensate fraction was also gathered for pairs of the same spin-species to confirm the presence or absence of induced p-wave superfluidity [66]. The values of the intra-spin condensate fraction were more than 10 orders of magnitude smaller than those for the inter-spin condensate fraction and were indistinguishable from zero at all pair momenta for both the spin-balanced case presented above and the spin-imbalanced cases discussed below.

4.2.2 Spin-imbalanced superconducting state

Having confirmed the accuracy of DMC simulations in the spin-balanced case, we now turn to the simplest class of spin-imbalanced systems with a 2:1 ratio of states on the Fermi surfaces, and so communal pairing theory predicts a $(N_\uparrow, N_\downarrow) = (2, 1)$ communal pairing instability while FFLO theory predicts pairs with nonzero net momentum. We conduct our study on the triangular lattice with 61 spin-up and 19 spin-down fermions, and in the square lattice with 25 spin-up and 9 spin-down fermions. On both lattices we use, $a = 6.0 r_s$ and $r_e = 0$.

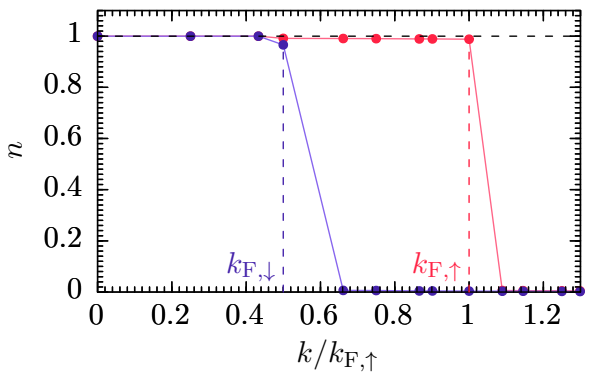

Fig. 4.2 Momentum density n of the majority up (red) and minority down (blue) spin-species on the triangular lattice, with momentum scaled in units of the majority species Fermi momentum. The vertical dashed lines indicate the respective Fermi momenta and the the horizontal black dashed line denotes $n = 1$. Both species exhibit the expected momentum density curves for pairing at their respective Fermi levels, with no evidence of breached superfluid formation or breaching of the Chandrasekhar-Clogston limit. The finite slope at the Fermi momenta are due to the finite resolution of the momentum space lattice. Similar results are observed on the square lattice.

Momentum density

We first examine the momentum density, with the results on the triangular lattice in Fig. 4.2. Both spin-species have momentum density close to unity beneath their respective Fermi momenta and close

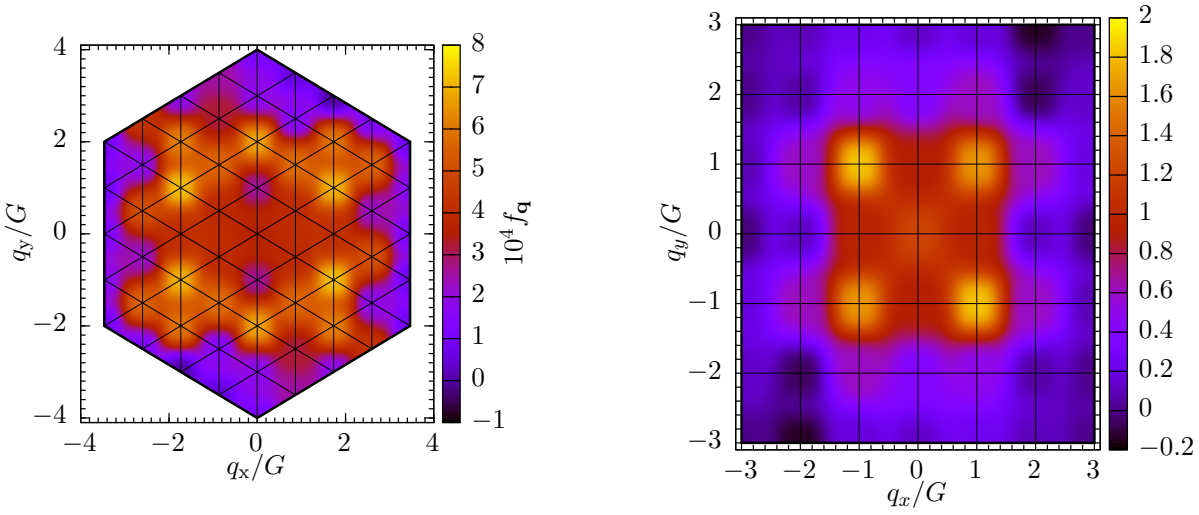

(a) Triangular lattice

(b) Square lattice

Fig. 4.3 Contour plot of the condensate fraction in momentum space for the spin-imbalanced case with 61 and 19 fermions of the majority and minority species respectively on the triangular lattice and 25 and 9 on the square lattice.

to zero above. A breached superfluid [28, 29, 67] would have the majority species exhibit depletion at the minority species Fermi momentum and a system crossing the Chandrasekhar-Clogston limit [68, 32] would have finite momentum density of the minority species at the majority species Fermi momentum, so it is clear that the system has not relaxed into either of those possible states. Knowing this, we can now move on to study the emergence of superconductivity by examining the condensate fraction.

Condensate fraction

The condensate fraction for the spin-imbalanced system with 61 majority and 19 minority species fermions is shown in Fig. 4.3a. Six major peaks in the condensate fraction are visible at the points 2 G units away from the origin, where G is the magnitude of the reciprocal lattice vector. This is the first observation in a first principles simulation of pairing at finite momentum in two or more dimensions and so could be the first numerical evidence of a FFLO or other exotic spatially modulated pairing phase, but not the BCS phase. The result is qualitatively consistent with the spatially modulated pairing phase observed in experimental [12] and numerical studies of one-dimensional systems [69], and with few-particle studies [36, 70]. We therefore now proceed to characterise the pairing to understand the correlations in the ground state.

The condensate fraction exhibits the six-fold rotational symmetry of the underlying momentum space lattice, in agreement with low temperature studies of spin-imbalanced pairing [71, 72] that predicts an increase in the number of pairing momenta, $\mathbf{q}$, in the ground state. However, a key characteristic of the DMC results in Fig. 4.3a is that they show statistically significant pairing at several momenta,

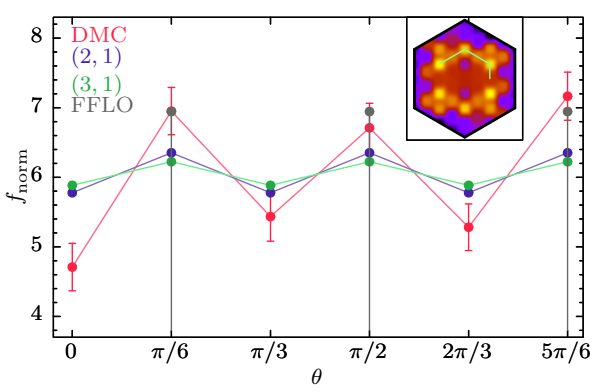

Fig. 4.4 Plot of normalised condensate fraction f_{norm} for states composed of pairs near the respective Fermi surfaces obtained using DMC (red) and predicted using exact diagonalisation assuming $(N_\uparrow, N_\downarrow) = (2,1)$ (blue), $(N_\uparrow, N_\downarrow) = (3,1)$ (green) and normal FFLO pairing with $(N_\uparrow, N_\downarrow) = (1,1)$ (grey) against angle of the pair momentum vector. Inset: a copy of Fig. 4.3a with a bright green curve indicating the displayed states of the plot.

$q < 4G$, that are not at the optimal magnitude predicted by FFLO theory, and decays radially. This is a significant departure as the family of FFLO theories [7, 8, 71, 72] predicts a single optimal magnitude of pairing momenta and zero pairing amplitude otherwise.

Similar results are seen in Fig. 4.3b where 25 majority and 9 minority fermions have been placed in a square lattice. The condensate fraction reflects the rotational symmetry of the underlying momentum space lattice, a feature shared with crystalline FFLO theories [71] and is nonzero beyond that of the optimal pairing momenta predicted by FFLO theory. While nonzero pairing at nonoptimal q is not present in FFLO theory or any of its derivatives, it is however consistent with communal pairing [1].

Characterisation of the communal state

The condensate fraction indicates that the superconducting correlations are consistent with communal pairing. To probe the nature and number of fermions in the communal pairing state, we follow the prescription of Ref. [36] and perform exact diagonalisation focusing on $(N_\uparrow, N_\downarrow) = (2,1)$ or $(3,1)$ fermions in a subset of the momentum states used in the DMC study, specifically those at the Fermi surfaces of the respective spin-species, and calculate the condensate fraction averaged across pair momenta of fixed q as a function of q.

The basis states chosen for the exact diagonalisation were such that in any particular basis state, all $N_\uparrow N_\downarrow$ possible pairs had equal magnitude of condensate fraction no matter the pairing vectors $\mathbf{q}$, allowing us to isolate, for example, the $(3,1)$ state from a $(2,1)$ state with non-contributing spin-up fermion. The contributions of the various basis states to the net ground state wavefunction then gives thecondensate fraction as a function of $\mathbf{q}$. The strength of the contact interaction for the exact diagonalisation study was chosen to match that used in the DMC study. Results are shown in Fig. 4.4 in the azimuthal direction and Fig. 4.5 radially, along with the averaged results obtained using DMC.

The red curve in Fig. 4.4 shows the condensate fraction obtained from DMC at the values of pair momentum indicated by the bright green line in the inset. These values were chosen as they are the ones which involve pairing of fermions at or near their respective Fermi momenta. The red curve in Fig. 4.5 shows the angle-averaged condensate fraction obtained from DMC, where the average is taken over all pair momenta of equal magnitude.

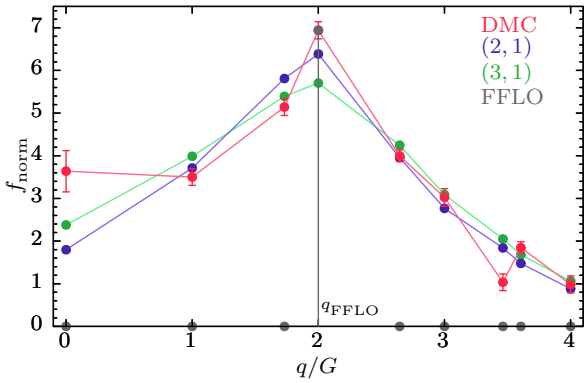

Fig. 4.5 Plot of normalised condensate fraction f_{norm} obtained using DMC averaged over q (red) and condensate fraction predicted using exact diagonalisation of the states beneath the respective Fermi surfaces assuming $(N_\uparrow, N_\downarrow) = (2,1)$ (blue), $(N_\uparrow, N_\downarrow) = (3,1)$ (green) and normal FFLO pairing with $(N_\uparrow, N_\downarrow) = (1,1)$ (grey) against q. The dashed black line marks out $q = q_{\text{FFLO}}$, the optimal magnitude of pairing momentum as predicted by FFLO theory and the only point on the FFLO curve where $f_{\text{norm}} \neq 0$.

The grey lines show the condensate fraction obtained when only one up and one down-spin fermion is allowed, as in the family of FFLO theories. FF theory predicts a single peak at a particular $\mathbf{q}$ [7], LO theory predicts two peaks at $\mathbf{q}$ and $-\mathbf{q}$ [8], and crystalline FFLO theory predicts multiple peaks for all $|\mathbf{q}| = q_{\text{FFLO}}$ [71, 72]. Our results confirm that having pre-selected for a single up and down-spin fermion, the crystalline FFLO ground state is the most stable out of these, in line with previous results [71, 72], with the condensate fraction equally shared by all symmetry related pair momentum vectors at this magnitude, as seen in Fig. 4.4. In the specific system studied here, $q_{\text{FFLO}} = 2G$, as seen in Fig. 4.5. To make a fair comparison between the DMC and exact diagonalisation results, we have normalized the condensate fraction obtained from exact diagonalisation so that the weighted squared deviation from the DMC results is minimized.

If instead communal pairing is considered, the results obtained from exact diagonalisation of both $(N_\uparrow, N_\downarrow) = (2,1)$ and $(3,1)$ are quantitatively similar to those obtained from DMC, with both sets of results exhibiting three key features. First and foremost, both have a nonzero condensate fraction at many values of q including $q = 0$, an essential feature of communal pairing theory that is in contrast to the predictions of FFLO theory. This is a direct consequence of considering non-exclusive communal pairing. Secondly, both DMC and communal pairing have a global maximum at $q = q_{\text{FFLO}}$ as this corresponds to the paired fermions being at their respective Fermi levels and thereby minimising their kinetic energy. Finally, both DMC and communal pairing curves exhibit a decay in the condensate fraction for $q > q_{\text{FFLO}}$ which is due to the increasing kinetic energy cost of the fermion pairs.

The quality of agreement between the communal pairing exact diagonalisation results and the DMC data can be quantified by the ratio of the weighted sum of squared deviations of the DMC results from either set of exact results in Fig. 4.4 (azimuthal) or Fig. 4.5 (radial), where the weights are the sample variances of the DMC data. This test statistic shows that the DMC results obtained are 27 times better described by an underlying $(N_\uparrow, N_\downarrow) = (3,1)$ communal state and 38 times better described by an underlying $(N_\uparrow, N_\downarrow) = (2,1)$ communal state than by FFLO pairing. This provides strong evidence that the state observed in DMC is not only communal, but has the appropriate values of $(N_\uparrow, N_\downarrow) = (2,1)$.

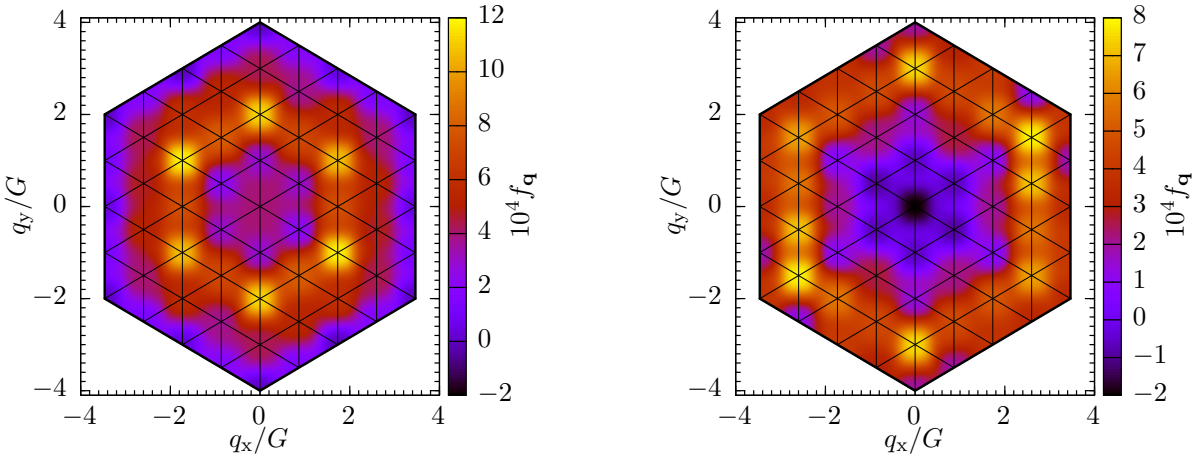

(a) 3:1

(b) 4:1

Fig. 4.6 Condensate fraction in momentum space for different ratios of majority to minority species fermions at the Fermi surfaces. 37 majority and 7 minority fermions create a 3:1 spin imbalance at the Fermi surfaces and 61 majority and 7 minority fermions create a 4:1 spin imbalance. The wavevectors are scaled in units of the respective reciprocal lattice vectors G, and black lines denote the q-space grid.

Similar results were obtained on performing exact diagonalisation at the Fermi surface of the system with 25 and 9 fermions on the square lattice; FFLO theory predicts a 4-fold degenerate peak at $q_{\mathrm{FFLO}} = \sqrt{2}G$ and zero condensate fraction otherwise while the communal exact diagonalisation results for $(N_\uparrow, N_\downarrow) = (2,1)$ and $(3,1)$ exhibited nonzero condensate over a range of momenta with a global maximum at q_{FFLO}. The test statistic obtained repeats the conclusion that the system is best described by a communal state with $(N_\uparrow, N_\downarrow) = (2,1)$.

The mismatch between the DMC and communal exact diagonalisation results, particularly at $q = 0$, may be due to a number of factors. Firstly, exact diagonalisation only accounts for a subset of the allowed momentum states without considering states above the Fermi surfaces, and secondly, that exact diagonalisation was carried out for only 2 (FFLO), 3 or 4 (communal) particles in total.

Changing spin-imbalance

Following on from our analysis of the 61 up-spin and 19 down-spin system, we now study two examples of greater spin-imbalance on a triangular lattice shown in Fig. 4.6. 37 majority and 7 minority fermions were used to create a 3:1 ratio at the Fermi surfaces with $a = 5.6$ and $r_{\mathrm{e}} = 0$. Peaks are clearly structured in a ring between $q = \sqrt{3}G$ and $q = 2G$ at 10 sample standard deviations above zero. Similarly, 61 majority and 7 minority fermions were used to create a 4:1 ratio at the Fermi surfaces with $a = 6.3$ and $r_{\mathrm{e}} = 0$, and the condensate fraction once again forms a ring structure peaked from $q = \sqrt{7}G$ to $q = \sqrt{12}G$ at 7 sample standard deviations above zero. Pairing FFLO peaks cannot be seen, and a BCS peak is even more strongly suppressed than in the 2:1 imbalanced case. These systems both provide further strong evidence of a spatially modulated superconducting order parameter, that is of the communal pairing

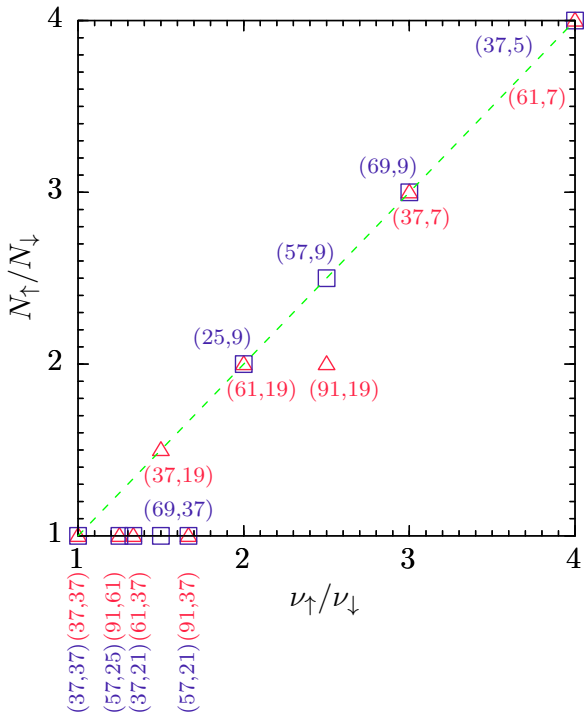

Fig. 4.7 Summary plot of the ratio of communal state indices $N_\uparrow/N_\downarrow$ to the ratio of densities of states at the respective Fermi surfaces, $\nu_\uparrow/\nu_\downarrow$. The red triangles indicate data taken on triangular momentum space lattices and the blue squares indicate data taken on square momentum space lattices. The bracketed number pairs indicate particle numbers for selected systems, with the colour corresponding to the respective lattice types. The line $N_\uparrow/N_\downarrow = \nu_\uparrow/\nu_\downarrow$ is indicated green.

rather than FFLO phase. A similar characterisation exercise to that described above with comparison to exact diagonalization was conducted on both systems and the communal state indices determined. The system with a 3:1 ratio is most closely described by a $(N_\uparrow, N_\downarrow) = (3,1)$ state and that with a 4:1 ratio by a $(N_\uparrow, N_\downarrow) = (4,1)$ state.

Relationship between $N_\uparrow/N_\downarrow$ and $\nu_\uparrow/\nu_\downarrow$

We have shown the results from four exemplar systems in detail to demonstrate the emergence of spatially modulated pairing and provided evidence that the form of the spatial modulation observed is characteristic of communal pairing. The analysis was also repeated for 14 systems with other Fermi surface ratios, for both the triangular and square lattices and at different system sizes, and the results analysed to ascertain the communal state indices, $N_\uparrow$ and $N_\downarrow$. A summary of the 18 sets of results obtained is shown in Fig. 4.7.

The relationship between the ratio of commmunal state indices $N_\uparrow/N_\downarrow$ and Fermi surface density of states ratios $\nu_\uparrow/\nu_\downarrow$ is well described by the line $N_\uparrow/N_\downarrow = \nu_\uparrow/\nu_\downarrow$, providing strong evidence for the communal pairing [36, 1] over FFLO. The relationship is particularly strong when the ratio can be written containing small integers [36] to minimise the product $N_\uparrow N_\downarrow$, mitigating the energy penalty for states with high $N_\uparrow N_\downarrow$ [1]. The correlation coefficient between the gathered data and the line $N_\uparrow/N_\downarrow = \nu_\uparrow/\nu_\downarrow$ is $R^2 = 0.95$.

4.2.3 Simulation parameters

It is of essential importance in any numerical study that the underlying distribution sampled from is well-behaved to ensure applicabaility of statistical measures such as sample variance. Here, histograms of the accumulated energy values from up to 10^7 samples did not reveal any evidence of non-normal behaviour and so the sample error is taken to be a good estimate of the true statistical error. We now explore the robustness of our conclusions against the choice of simulation parameters, specifically the pseudopotential cutoff length, the DMC timestep, and the number of DMC walkers. The system was selected to have 61 majority and 19 minority spin fermions.

Pseudopotential cutoff length The effect of altering the cutoff length L_C of the UTP on the DMC energy was investigated with results shown in Fig. 4.8. In contrast to theoretical predictions, the DMC energy, E_{DMC}, is shown to vary considerably with L_C, with high E_{DMC} at low L_C and vice versa, with an intermediate plateau. All data were gathered with a trial wavefunction that had the same number of variational parameters in the pairing orbital and the Jastrow factor, optimised for the specific potentials, with all other simulation parameters constant.

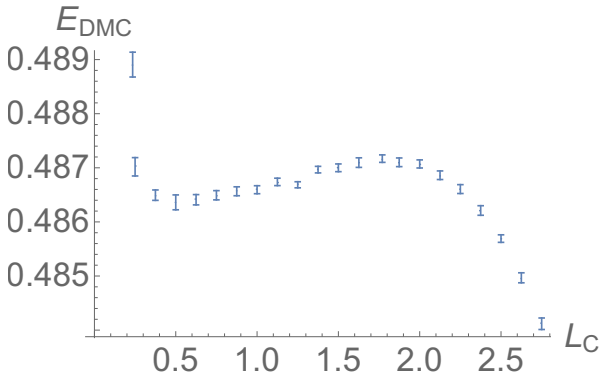

Fig. 4.8 Graph of DMC energy, E_{DMC}, against cutoff length L_C of the pseudopotential. The energy is shown to vary considerably with cutoff length. At low L_C, E_{DMC} increases as a deeper, more rapidly varying UTP increases the variance. At high L_C, E_{DMC} decreases as three-body and higher interactions become more common.

The high E_{DMC} values obtained for low L_C are primarily due to poor fit of wavefunction; as a low L_C leads to a deep and rapidly varying UTP over a smaller region of space, the trial wavefunction should also include higher order terms to reflect the rapid variation of the UTP. Limiting the number of variational parameters in order to make the results more easily comparable thus leads to a poorer fit of wavefunction as L_C decreases, resulting in the ground state not being adequately projected by DMC and increasing the energy. In addition, the deep, rapidly varying UTP results in a greater spread of values for the local energy, leading to a higher sample variance. For $L_C = 0.125 r_s$ (not in figure), the variation in local energies was wild enough that it eventually lead to extinction of all walkers through the DMC branching factor, and as such no data could be gathered under the simulation parameters selected for all other values of L_C.

The low E_{DMC} values obtained for high L_C in contrast are due to higher order interactions beyond pairing, as the UTP now extends over a large enough region that the formation of larger correlated structures is possible. These higher order interactions further decrease the energy and indicate a

breakdown of the UTP's ability to emulate a contact interaction, which should only result in pair point interactions for a reasonable fermion density.

It is desirable to have an easily optimised wavefunction with a low variance and no evidence of three body effects. Therefore, an intermediate value of $L_C = r_s$ was chosen for all other tests and simulations.

DMC timestep The DMC algorithm is only exact in the limit of zero timestep τ. However, the computational time required to achieve a given error bar on the energy scales as $1/\tau$, so it is not feasible to simply use infinitesimally small timesteps. That is, for a given allotment of computer time, a smaller timestep leads to a more accurate measure of the energy on average but sacrifices precision. For sufficiently small τ, the DMC energy varies linearly with the timestep, $E_{\mathrm{DMC}}(\tau) = E_0 + \kappa\tau$ where E_0 is the true ground state energy. Hence, if the linear regime can be identified, it is possible to extrapolate the DMC results down to zero timestep, and efficient algorithms have been proposed for this [73–75].

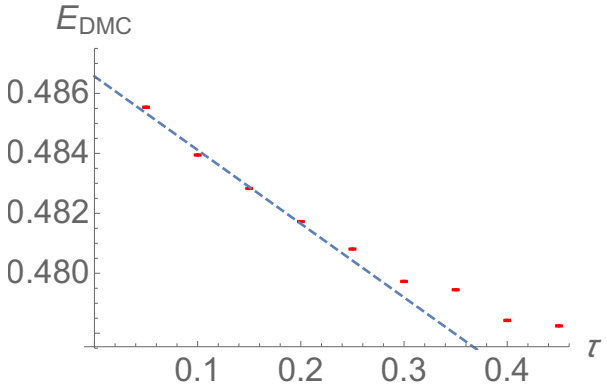

Fig. 4.9 Graph of DMC energy E_{DMC} against DMC timestep τ. Raw data is presented in red with a best fit line in dashed blue. The linear regime of E_{DMC} is identified as $\tau < 0.20$ and indicates a $\tau = 0$ limit of 0.48657(2) for the energy. E_{DMC} at each point was calculated from 50000 samples.

We follow the algorithm in [74] to extrapolate to zero timestep using the results shown in Fig. 4.9. Taking the maximum timestep of the linear regime to be $\tau_2 = 0.20$, we set $\tau_1 = \tau_2/4$, and use a total number of steps $T_1 = 2.5 \times 10^7$ and $T_2 = T_1/8 = 3.125 \times 10^6$ respectively to obtain an energy of 0.48684(2).

DMC walkers The DMC algorithm makes use of the drift-diffusion of a regulated number of walkers for a specified amount of time to obtain expectation values of physical observables. The total computation time T therefore is a function of not only the time-averaged number of DMC walkers, W_{DMC}, but also of the number of timesteps, N, as $T = W_{\mathrm{DMC}}N$. The effect of varying W_{DMC} while keeping T constant was investigated and the results shown in Fig. 4.10. The DMC energy does not vary significantly even as W_{DMC} spans several orders of magnitude while the sample variance decreases for $W_{\mathrm{DMC}} > 2000$. It is thus preferable to have a high number of walkers propogated a few steps forward in imaginary time than to have a small number of walkers propogate for a long imaginary time.

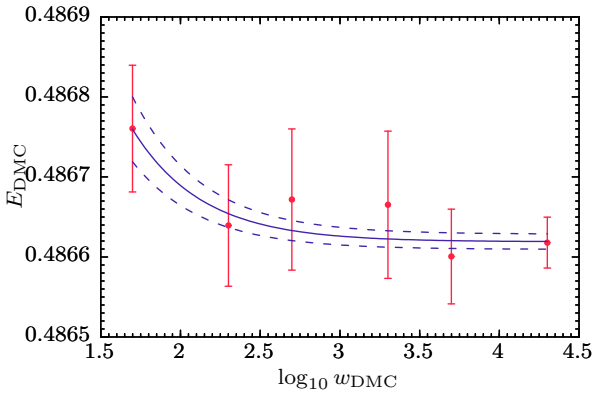

Fig. 4.10 Graph of DMC energy E_{DMC} against the Log of the number of DMC walkers W_{DMC} for a fixed product of the number of walkers and number of steps, $W_{\mathrm{DMC}}N = 2.5 \times 10^7$.

4.3 Conclusions

We have observed a spatially modulated superconducting state using DMC. Furthermore, the state is qualitatively different from an FFLO state [7, 8], having condensate fraction peaks at multiple momenta, as opposed to the single peak expected for FFLO. Exact diagonalisation studies provide corroborating evidence that the distribution of condensate fraction with momenta is more indicative of communal superconductivity [36, 1] than traditional FFLO or crystalline FFLO superconductivity [71, 72]. We have confirmed convergence of the state with respect to choices of system size, pseudopotential cutoff length, DMC timestep, and DMC walker population.

This numerical evidence that builds on previous analytical work [1, 36] provides an interesting challenge for experiments to observe the communal state in physical systems. In real space the superconducting order parameter will exhibit a beat pattern due to the interference between similar q-vectors, which could allow the identification of the particular q-vectors in the superconductor. The order parameter and its spread in momentum could be determined in an ultracold atomic gas experiment through density-density correlations measured from time-of-flight experiments [76]. In contrast, FFLO and crystalline FFLO theories predict sharp peaks in the condensate fraction, as in spin-balanced BCS theory, at fixed magnitude of the pairing momenta.

Additionally, as the communal number pair $(N_\uparrow, N_\downarrow)$ is a function of the spin imbalance, multiple phase transitions through several superconducting phases should be observed as the imbalance is increased. Each transition is expected to be second order, and so the communal superconducting phase would be characterized by a series of singularities in the heat capacity and the compressibility, which should be directly observable in ultracold atomic gases [77] as the spin-imbalance is changed. No such phase transitions are expected for the FFLO phase at fixed temperature.

An orthogonal line of questioning that may be of concern in real experiments is on the possible effects a nonzero effective range might have on the obtained results. Previous work [78] suggests that the obtained energy differences from the noninteracting state should increase towards zero, the condensate fraction should be constant over a wide range of scattering lengths, and the momentum density should become more sharply step-like.

Finally, the match with exact diagonalisation studies provides evidence that the elementary excitations above the proposed ground state are well-described by the few fermion analysis [36]. This should have novel consequences especially concerning Andreev reflection experiments as the strong correlations between a group of fermions held in a communal state should result in a range of retroreflected hole momenta for a single incident fermion, in sharp contrast to the single hole momentum per fermion expected in normal FFLO theory.

Chapter 5

Quantum fluctuations

The preceding two chapters dealt with the analytic motivation and numerical verification respectively of communal pairing theory in the context of spin-imbalanced systems. The question naturally arises therefore of whether any of the insights gained from those studies might carry over to the spin-balanced system as a modification to the well-established BCS theory. This chapter was submitted for publication in Physical Review A and is pending acceptance. The analytical work presented is my own with Dr. Conduit providing valuable discussion and help editing the paper.

The microscopic description of superconductivity by Bardeen, Cooper, and Schrieffer (BCS) [4] is one of the historic milestones of condensed matter physics, accurately describing a host of materials [79–82], and serving as the foundation for numerous theoretical extensions and numerical studies, such as Eliashberg theory [83], FFLO theory [7, 8], breached superconductivity [28, 29, 67], the T-matrix formulation of the BEC-BCS crossover [84], quantum Monte Carlo studies of the weakly interacting [85] and unitarity limits [86], studies on the effects of mass imbalances [87, 88], 3-body effects [89] and the more recent communal pairing theory [36, 1]. Central to the usual formulation of BCS theory is the assumption that the Cooper pairs condense only in the zero net momentum state, an assumption that is challenged by communal pairing theory [36, 1, 2].

Communal pairing theory as originally derived [36] showed that it is energetically favourable for Cooper pairs to share fermions. By considering the quantities N_σ with $\sigma \in \{\uparrow,\downarrow\}$, where $N_\uparrow$ is the number of up-spin fermions any particular down-spin fermion is paired with, and *vice versa*, communal pairing theory predicts an optimal ratio of communal state indices of $N_\uparrow/N_\downarrow = 1$ for the spin-balanced BCS system and $N_\uparrow/N_\downarrow \neq 1$ in a spin-imbalanced system [1, 2]. The central paradigm shift that a finite gap may be present at non-optimal pairing momenta allows $N_\uparrow$ and $N_\downarrow$ to be greater than 1. It is therefore natural to ask whether as interactions get stronger in a spin-balanced BCS system, multiple Cooper pairs will share fermions, $N_\uparrow > 1$ and $N_\downarrow > 1$, to increase correlations. The variational principle ensures that the inclusion of additional freedom to form correlations will certainly not increase the ground state energy so can only lower it.

This chapter explores the extent of communality on spin-balanced systems. We do this by extending BCS theory, complementary to other additional effects, such as retardation as in Eliashberg theory [83]

or induced Gor'kov-Melik-Barkhudarov interactions (GMB) [19, 51]. We will focus our discussion on 2D systems as communality is predicted to be enhanced in low dimensions [36, 1, 2] and because the results may be derived analytically here, but will also derive equivalent 3D results where possible. We will also be pre-emptively setting $N_\uparrow = N_\downarrow = N_q$ to reflect the fact that the system is spin-balanced.

In the next section we briefly recap conventional superconductivity from a field theoretic perspective and note the main difficulty with an exact treatment. Section 5.2 analyses single superconducting channels, making a distinction between static and oscillating channels before we combine these results into a minimally coupled model of multiple active superconducting channels in Section 5.3, making clear the connection to the BEC-BCS crossover. Conclusions are summarised in Section 5.4.

5.1 Quantum action

To start our analysis from a secure theoretical footing, we analyse the quantum partition function of a fermion gas with attractive contact interactions of strength g, $\mathscr{Z} = \int \mathscr{D}\bar{\psi}\mathscr{D}\psi \exp(-S[\bar{\psi},\psi])$, where

$$S[\bar{\psi},\psi] = \int \mathrm{d}\tau \mathrm{d}x \left[\sum_\sigma \bar{\psi}_\sigma (\partial_\tau - \frac{\nabla^2}{2m} - \mu)\psi_\sigma - g\bar{\psi}_\uparrow \bar{\psi}_\downarrow \psi_\downarrow \psi_\uparrow \right],$$

is the quantum action, ψ is a Grassman field with $\bar{\psi}$ its conjugate, τ the imaginary time goes from 0 to β the inverse temperature, and $\sigma \in \{\uparrow,\downarrow\}$ denotes the spin-species. The fermions are of equal mass m and we work in Hartree units so $\hbar = k_\mathrm{B} = 1$. A Hubbard-Stratonovich decoupling in the Cooper channel yields the modified action

$$S[\bar{\psi},\psi,\Delta^*,\Delta] = \int \mathrm{d}\tau \mathrm{d}x \left(\sum_\sigma \bar{\psi}_\sigma (\partial_\tau - \frac{\nabla^2}{2m} - \mu)\psi_\sigma - \Delta\bar{\psi}_\uparrow\bar{\psi}_\downarrow - \Delta^*\psi_\downarrow\psi_\uparrow + \frac{\Delta^*\Delta}{g} \right),$$

where the gap parameter is defined as $\Delta \equiv g\langle\psi_\downarrow\psi_\uparrow\rangle$ and is a function of both space x and time τ. The Fourier transform of the gap is therefore generically a function of the pair momentum $\mathbf{q}$ and the frequency Ω, which label the various superconducting channels. In the weakly interacting limit, the gap is known to be isotropic and static and therefore the Fourier transform is a delta function in the momentum-frequency domain. However, in the strongly interacting limit, approaching the BEC-BCS crossover, communal pairing allows Cooper pairs to share fermions [36]. We note there is an analogy to Cooper pairs becoming confined in real space, which should correspond to a widening of the gap in momentum space. It is this width that is the central concern of this chapter, and so we Fourier transform

to momentum and frequency space to obtain the action

$$\begin{aligned} S[\bar{\psi},\psi,\Delta^*,\Delta] =& \beta \sum_{\mathbf{k},\omega,\sigma} \bar{\psi}_{\mathbf{k},\omega,\sigma}(-\mathrm{i}\omega+\xi_{\mathbf{k}})\psi_{\mathbf{k},\omega,\sigma} \\ & -\beta \sum_{\mathbf{k},\mathbf{q},\omega,\Omega} \left(\Delta_{\mathbf{q},\Omega}\bar{\psi}_{\mathbf{k}+\frac{\mathbf{q}}{2},\omega+\frac{\Omega}{2},\uparrow}\bar{\psi}_{-\mathbf{k}+\frac{\mathbf{q}}{2},-\omega+\frac{\Omega}{2},\downarrow} + \mathrm{h.c.}\right) \\ & +\beta \sum_{\mathbf{q},\Omega} \frac{\left|\Delta_{\mathbf{q},\Omega}\right|^2}{g}, \end{aligned}$$

where $\mathbf{k}$ and $\mathbf{q}$ label momenta and pair momenta respectively, ω is a fermionic matsubara frequency, Ω is a bosonic matsubara frequency, $\xi_{\mathbf{k}} \equiv |\mathbf{k}|^2/2m-\mu$ is the free particle dispersion less the chemical potential, $\Delta_{\mathbf{q},\Omega} = g\langle\sum_{\mathbf{k},\omega}\psi_{\mathbf{k}+\frac{\mathbf{q}}{2},\omega+\frac{\Omega}{2},\downarrow}\psi_{-\mathbf{k}+\frac{\mathbf{q}}{2},-\omega+\frac{\Omega}{2},\uparrow}\rangle$ are the Fourier components of the gap function and h.c. denotes the Hermitian conjugate.

We will ultimately consider communal pairing through multiple channels but to lay the foundation of the analysis, and connect to standard BCS theory, we will first decouple through a single $\Delta_{\mathbf{q},\Omega}$ channel.

5.2 Decoupling in a single channel

We first follow the standard BCS prescription to permit each fermion to be paired with only one opposite spin fermion. Therefore, only one superconducting channel $\Delta_{\mathbf{q},\Omega}$ is nonzero, revealing a key difference between the channels where $\Omega = 0$ and $\Omega \neq 0$, namely that while the action of the static channels is fully real, the oscillating channels have a complex action indicating a finite lifetime of the Cooper pairs. These different situations are dealt with in Subsections 5.2.1 and 5.2.2 respectively. These decoupled expressions for the action will in Section 5.3 be combined to provide a full action where each fermion may be paired with every other.

With $\Delta = 0$ except at a specific $\mathbf{q}$ and Ω, the momentum sum in the three point interaction terms is simplified. The action is then

$$S_{\mathbf{q}}[\bar{\psi},\psi,\Delta^*,\Delta] = \beta\frac{\left|\Delta_{\mathbf{q},\Omega}\right|^2}{g} + \beta\sum_{\mathbf{k},\omega}\bar{\boldsymbol{\psi}}^{\mathrm{T}}_{\substack{\mathbf{k},\mathbf{q}\\ \omega,\Omega}}\begin{pmatrix} G^{-1}_{\mathbf{k}+\frac{\mathbf{q}}{2},\omega+\frac{\Omega}{2},\uparrow} & -\Delta_{\mathbf{q},\Omega} \\ -\Delta^*_{\mathbf{q},\Omega} & G^{-1}_{-\mathbf{k}+\frac{\mathbf{q}}{2},-\omega+\frac{\Omega}{2},\downarrow}\end{pmatrix}\boldsymbol{\psi}_{\substack{\mathbf{k},\mathbf{q}\\ \omega,\Omega}},$$

where $\bar{\boldsymbol{\psi}}^{\mathrm{T}}_{\substack{\mathbf{k},\mathbf{q}\\ \omega,\Omega}} \equiv \begin{pmatrix}\bar{\psi}_{\mathbf{k}+\frac{\mathbf{q}}{2},\omega+\frac{\Omega}{2},\uparrow} & \psi_{-\mathbf{k}+\frac{\mathbf{q}}{2},-\omega+\frac{\Omega}{2},\downarrow}\end{pmatrix}$ and the inverse propagator $G^{-1}_{\mathbf{p},\nu,\sigma} \equiv \sigma(-\mathrm{i}\nu+\xi_{\mathbf{p}})$. The fermion fields can then be integrated out to obtain the effective action

$$S_{\mathbf{q},\Omega}[\Delta^*,\Delta] = \beta\frac{\left|\Delta_{\mathbf{q},\Omega}\right|^2}{g} - \sum_{\mathbf{k},\omega}\ln\left(1-\left|\Delta_{\mathbf{q},\Omega}\right|^2 G_{\mathbf{k}+\frac{\mathbf{q}}{2},\omega+\frac{\Omega}{2},\uparrow}G_{-\mathbf{k}+\frac{\mathbf{q}}{2},-\omega+\frac{\Omega}{2},\downarrow}\right), \tag{5.1}$$

where we have set the energy of the noninteracting system to be our zero reference.

Far below the critical temperature, and for $q^2/2m + \Omega^2/4\mu < \left|\Delta_{\mathbf{q},\Omega}\right|^2/\mu$, we may perform the Matsubara summation to obtain

$$S_{\mathbf{q},\Omega}[\Delta^*,\Delta] = \beta\frac{\left|\Delta_{\mathbf{q},\Omega}\right|^2}{g} - \beta\sum_{\mathbf{k}}\left(E_{\mathbf{k},\mathbf{q},\Omega} - \varepsilon_{\mathbf{k},\mathbf{q},\Omega}\right), \tag{5.2}$$

where $E_{\mathbf{k},\mathbf{q},\Omega} \equiv \sqrt{\left|\Delta_{\mathbf{q},\Omega}\right|^2 + \varepsilon^2_{\mathbf{k},\mathbf{q},\Omega}}$, $\varepsilon_{\mathbf{k},\mathbf{q},\Omega} \equiv \frac{k^2}{2m} + \frac{q^2}{8m} - \mu - \mathrm{i}\frac{\Omega}{2}$, and θ is the angle between $\mathbf{k}$ and $\mathbf{q}$. The limit on the magnitude of $\mathbf{q}$ is heuristically where the kinetic energy of the Cooper pair center of mass overcomes the superconducting condensation energy and therefore breaks the pair. Likewise, the limit on Ω sets a maximum allowed frequency of temporal oscillations of the gap. This therefore limits the stability of a finite $\Delta_{\mathbf{q},\Omega}$ solution. The action has a leading order temperature dependence of the form $f(\beta,q,\Omega)\left|\Delta\right|^2 \mathrm{e}^{-\beta|\Delta|}$ where f is some bounded function. The term tends to zero as $T \to 0$.

The first and second terms that remain at zero temperature require the contact interaction strength g be regularized to eliminate the ultraviolet divergence. We replace g with the s-wave scattering length a_s via the formal substitution [39, 40, 38]

$$\frac{1}{g} = \begin{cases} mL^2\left(\frac{1}{2\pi}\ln\kappa a + \frac{1}{L^2}\sum_{\mathbf{k}}\frac{1}{k^2-\kappa^2}\right), & D=2, \\ mL^3\left(-\frac{1}{4\pi a_\mathrm{s}} + \frac{1}{L^3}\sum_{\mathbf{k}}\frac{1}{k^2}\right), & D=3, \end{cases} \tag{5.3}$$

where L is the system length, $a = \frac{\mathrm{e}^\gamma}{2}a_\mathrm{s}$ is the scattering length scaled for convenience with γ the Euler—Mascheroni constant, and κ is an unimportant momentum scale that will vanish once the regularisation procedure is carried out in full. The scattering length a (or a_s) may be directly controlled experimentally [90–92]. This formal substitution works to regularise the integrals of Eq. (5.2) at any value of Ω.

The ultraviolet divergence of Eq. (5.2) is thus exactly cancelled, allowing us to take the sum over all $\mathbf{k}$. Additionally, the first term on the right hand side of the regularization in Eq. (5.3) allows us to predict that the familiar exponential suppression factor $\mathrm{e}^{-2/g\nu_\mathrm{F}}$ seen in the solid-state BCS gap will be replaced with $1/k_\mathrm{F}a$ in 2D and $\mathrm{e}^{\pi/2k_\mathrm{F}a_\mathrm{s}}$ in 3D.

The action in 2D can be resolved analytically as

$$S_{\mathbf{q},\Omega} = -\frac{\beta mL^2}{4\pi}\left[\mu_{q,\Omega}\left(\sqrt{\left|\Delta_{\mathbf{q},\Omega}\right|^2 + \mu^2_{q,\Omega}} - \mu_{q,\Omega}\right) - \left|\Delta_{\mathbf{q},\Omega}\right|^2 \ln\frac{ma^2}{\sqrt{\mathrm{e}}}\left(\sqrt{\left|\Delta_{\mathbf{q},\Omega}\right|^2 + \mu^2_{q,\Omega}} - \mu_{q,\Omega}\right)\right], \tag{5.4}$$

where $\mu_{q,\Omega} \equiv \mu - \frac{q^2}{8m} + \mathrm{i}\frac{\Omega}{2}$ and we have neglected the finite temperature correction term. In 3D, the action may be evaluated in terms of an elliptic integral

$$S^{(3\mathrm{D})}_{\mathbf{q},\Omega} = -\frac{\beta mL^3}{\pi^2}\left[\frac{\pi\left|\Delta^{(3\mathrm{D})}_{\mathbf{q},\Omega}\right|^2}{4a_\mathrm{s}} + \sqrt{2m\mu^{(3\mathrm{D})5}_{q,\Omega}}I_1\left(\frac{\left|\Delta^{(3\mathrm{D})}_{\mathbf{q},\Omega}\right|}{\mu^{(3\mathrm{D})}_{q,\Omega}}\right)\right],$$

where $I_1(z) \equiv \int_0^\infty \mathrm{d}x x^2(\sqrt{z^2+(x^2-1)^2}-(x^2-1)-z^2/2x^2)$ is a dimensionless function.

Now that we have derived an expression for the action we are well positioned to consider separately two cases, firstly the special case of $\Omega = 0$ before extending this to the finite Ω system.

5.2.1 Static single channel

The static action can be found by setting $\Omega = 0$ in Eq. (5.4) to obtain

$$S_{\mathbf{q}} = -\frac{\beta m L^2}{4\pi}\left[\mu_q\left(\sqrt{|\Delta_{\mathbf{q}}|^2+\mu_q^2}-\mu_q\right)-|\Delta_{\mathbf{q}}|^2\ln\frac{ma^2}{\sqrt{\mathrm{e}}}\left(\sqrt{|\Delta_{\mathbf{q}}|^2+\mu_q^2}-\mu_q\right)\right],$$

where we drop the Ω subscript entirely as it is understood to be zero. The action is a real number, confirming that the condensed phase is stable in time. We will now obtain the grand potential through the standard formula $\Phi = -T\ln\mathscr{Z}$, the gap $\Delta_{\mathbf{q}}$, and the chemical potential that promote a platform for our future analysis and allow us to compare to standard results.

Grand potential The grand potential $\Phi_{\mathbf{q}}$ is obtained directly from the action

$$\Phi_{\mathbf{q}} = -\frac{mL^2}{4\pi}\left[\mu_q\left(\sqrt{|\Delta_{\mathbf{q}}|^2+\mu_q^2}-\mu_q\right)-|\Delta_{\mathbf{q}}|^2\ln\frac{ma^2}{\sqrt{\mathrm{e}}}\left(\sqrt{|\Delta_{\mathbf{q}}|^2+\mu_q^2}-\mu_q\right)\right]. \tag{5.5}$$

As expected, the grand potential tends to that of the normal state when $|\Delta_{\mathbf{q}}| = 0$. In 3D the form of the grand potential similarly mirrors the 3D action without a factor of β

A subtlety that bears mention is that in both 2D and 3D the expression above requires $q^2/2m < |\Delta_{\mathbf{q}}|^2/\mu$, that is when the additional kinetic energy of a Cooper pair is less than the condensation energy. Above that limit, the additional kinetic energy is sufficient to break the Cooper pairs and so the grand potential evaluates to zero identically.

Superconducting gap The gap is determined by requiring that the grand potential be stationary with respect to the gap, $\frac{\partial\Phi}{\partial\Delta_{\mathbf{q}}^*} = 0$, giving the gap

$$\Delta_{\mathbf{q}} = \begin{cases} \frac{1}{ma^2}\sqrt{1+2ma^2\mu_q} & q < \frac{2}{a} \\ 0 & q \geq \frac{2}{a}. \end{cases} \tag{5.6}$$

The gap in 3D meanwhile is the solution of the implicit equation

$$-\frac{1}{k_{\mathrm{F}}a_{\mathrm{s}}} = \frac{2}{\pi}\sqrt{\frac{\mu_q^{(3\mathrm{D})}}{E_{\mathrm{F}}}}I_2\left(\frac{\left|\Delta_{\mathbf{q}}^{(3\mathrm{D})}\right|}{\mu_q^{(3\mathrm{D})}}\right), \tag{5.7}$$

where $I_2(z) \equiv \int_0^\infty \mathrm{d}x(x^2/\sqrt{z^2+(x^2-1)^2}-1)$.

Solving for μ The chemical potential μ is found from the equation $N = -\frac{\partial\Phi}{\partial\mu}$. In 2D it is then

$$\mu = E_{\mathrm{F}}\left(1 - \frac{1}{k_{\mathrm{F}}^2 a^2} + \frac{q^2}{4k_{\mathrm{F}}^2}\right),$$

and that depends on the net momentum of the condensed Cooper pairs, owing to their kinetic energy.

In 3D we recast the BCS number equation [38] to obtain

$$1 = \frac{3}{2}\sqrt{\frac{\mu_q^{(3\mathrm{D})}}{E_{\mathrm{F}}}}^3 I_3\left(\frac{\left|\Delta_{\mathbf{q}}^{(3\mathrm{D})}\right|}{\mu_q^{(3\mathrm{D})}}\right), \tag{5.8}$$

where $I_3(z) \equiv \int_0^\infty \mathrm{d}x x^2\left[1 - (x^2-1)/\sqrt{z^2+(x^2-1)}\right]$. Since the pair of coupled Eqns. (5.7) and (5.8) only depend implicitly on $\mathbf{q}$ through $\Delta_{\mathbf{q}}^{(3\mathrm{D})}$ and $\mu_q^{(3\mathrm{D})}$, we conclude that $\mu_q^{(3\mathrm{D})} = \mu_{\mathrm{BCS}}^{(3\mathrm{D})}$ and therefore $\mu^{(3\mathrm{D})} = \mu_{\mathrm{BCS}}^{(3\mathrm{D})} + \frac{q^2}{8m}$. At $q = 0$ the forms of Equations (5.7) and (5.8) are indeed equivalent to those of the regularized BCS equations [38].

Weak interactions We study the weakly interacting limit in 2D by setting $k_{\mathrm{F}}a \gg 1$. In this limit, $\mu_q \approx E_{\mathrm{F}}$ as expected and the gap reduces to $\Delta_{\mathbf{q}} \approx 2E_{\mathrm{F}}/k_{\mathrm{F}}a$ from which we may extract the 3D analogue $\Delta_{\mathbf{q},(3\mathrm{D})} \sim E_{\mathrm{F}}\mathrm{e}^{-\pi/2k_{\mathrm{F}}|a_{\mathrm{s}}|}$ by inspection of the regularisation procedure in Eq. (5.3), which agrees with standard BCS theory [38]. Similarly, we can state that in the weakly interacting limit the validity requirement $\frac{q^2}{2m} < \frac{|\Delta_{\mathbf{q}}|^2}{\mu}$ takes the form $q < \frac{8k_{\mathrm{F}}}{\mathrm{e}^2}\mathrm{e}^{-\pi/2k_{\mathrm{F}}|a_{\mathrm{s}}|}$.

5.2.2 Oscillating single channel

When Ω is nonzero, the action $S_{\mathbf{q},\Omega}$ is complex. Expanding the 2D expression of Eq. (5.4) in small Ω about our static $\Omega = 0$ solution, we obtain

$$S_{\mathbf{q},\Omega} = S_{\mathbf{q},0} - \mathrm{i}\frac{\beta m L^2}{4\pi}\left(\sqrt{|\Delta_{\mathbf{q},\Omega}|^2 + \mu_{q,0}^2} - \mu_{q,0}\right)\Omega + \mathscr{O}\left(\Omega^2\right).$$

As $S_{\mathbf{q},0}$ is real, the imaginary part of $S_{\mathbf{q},\Omega}$ is linear in Ω. All terms of order Ω^2 and higher are proportional to at least the second power of $|\Delta_{\mathbf{q},\Omega}|$. The imaginary part of the action corresponds to the spontaneous decay rate of Cooper pairs condensed in this superconducting channel, $\Gamma_{\mathbf{q},\Omega}^{\mathrm{sd}} = |\Im S_{\mathbf{q},\Omega}|$. In 3D, the action may be likewise expanded in the low-Ω limit to obtain an imaginary part of the action linear in Ω.

In this section we have decoupled in a single channel, performing a BCS-like analysis of the resulting simplified action for general pair momentum $\mathbf{q}$ and frequency Ω. Two broad conclusions follow from this analysis. Firstly, when $\Omega = 0$, multiple $\mathbf{q}$ channels are stable with identical nonzero gap magnitude and equal grand potential. This should be observable in weakly interacting superconductors and can be understood as the system admitting a persistent supercurrent, provided the pair moves slowly enough that dissipation through quasiparticle excitation is not energetically feasible. Secondly, for $\Omega \neq 0$, the action

develops an imaginary term, limiting the lifetime of oscillating modes. This may be thought of as an inductance that promotes stability of gap-dependent macroscopic observables, such as the supercurrent.

5.3 Multiple channels

The results of the previous section indicate that in principle, multiple channels are stable at any particular scattering length, which naturally begs the question of whether multiple channels coexist in the ground state. Such communal superconductivity has previously been analyzed and explored numerically in spin-imbalanced systems [1, 2] and so it is natural to now look at spin-balanced systems. We will introduce the variational freedom to explore these multiple active channels with the communal parameter $N_q = \sum_{\mathbf{q}} 1$, the number of $\mathbf{q}$ channels with nonzero gap. Clearly, N_q is at least equal to 1 (standard BCS superconductor) and is bounded from above by one of two physical arguments that in 2D take the form,

$$N_q < \min\left(1 + \frac{2N}{k_{\mathrm{F}}^2 a^2}, \frac{N}{2}\right),$$

where the first limit (weakly interacting) corresponds to all superconducting channels for which $q < 2/a$ active and is exactly equivalent to the physical limit $q^2/2m < |\Delta_{\mathbf{q}}|^2/\mu$ mentioned previously, with the second limit (strongly interacting) that there are only $N/2$ choices of pairing partner for each fermion. The crossover is at $k_{\mathrm{F}}a = 2$. We note for completeness that in 3D the first limit has the form $N_q = 1 + N q_{\max}(a_{\mathrm{s}})^3/2k_{\mathrm{F}}^3$ where $q_{\max}(a_{\mathrm{s}}) = \sqrt{2m/\mu(a_{\mathrm{s}})}\,|\Delta_{\mathbf{q}}(a_{\mathrm{s}})|$ and the second limit is unchanged.

In addition to this new communal variational freedom, we will also consider the effect on the grand potential of the short-lived finite Ω modes, where quantum fluctuations of the temporally oscillating modes can contribute to driving communal ordering of the superconducting gap. This contribution will then be added to a minimal model of multiple active static $\Omega = 0$ modes. We therefore calculate the total quantum partition function as $\mathscr{Z} = \mathscr{Z}_0 \mathscr{Z}_{\Omega\neq 0}$, where $\mathscr{Z}_0$ gives the multi-channel saddle point approximation and $\mathscr{Z}_{\Omega\neq 0}$ accounts for temporal fluctuations of the various modes. The partition function allows us to find the grand potential and differentiate to obtain the expected value of the number of fermions shared between Cooper pairs, N_q, and then explore the evolution of N_q as we approach the BEC-BCS crossover. We tackle the static and fluctuating contributions in order.

5.3.1 Static channels

We first focus on the static $\Omega = 0$ channels. The static part of the partition function has the form

$$\mathscr{Z}_0 = \exp\left[-\beta \frac{1}{N_q} \sum_{\mathbf{q}} \Phi_{\mathbf{q}}(\Delta_{\mathbf{q}}, \mu)\right], \tag{5.9}$$

which accounts for the long-lived, $\Omega = 0$ channels where a $|\Delta_{\mathbf{q},0}| \neq 0$ mean-field solution is possible. The channels are coupled as they draw from the same reservoir of fermions with common chemical potential μ. The averaging over modes may be understood in the context of the quantum action as

considering each fermion as being paired to multiple opposite-spin fermions probabilistically, and all channels are equally weighted since the grand potential of each channel in the single channel decoupling is identical. The mean-field grand potential is then

$$\begin{aligned}\Phi_0 &= \frac{1}{N_q}\sum_{\mathbf{q}}\Phi_{\mathbf{q}}(\Delta_{\mathbf{q}},\mu)\\ &= -\frac{E_{\mathrm{F}}L^2(1+2ma^2\mu)^2}{4\pi k_{\mathrm{F}}^2a^4}+\frac{E_{\mathrm{F}}(N_q-1)^2}{4N_qk_{\mathrm{F}}^2a^2},\end{aligned} \tag{5.10}$$

that is, a sum over the grand potentials of single channel superconductors. The contribution from oscillating channels does not depend on the magnitudes of the static channels and so we may find the superconducting gap in the same way as for the single channel, by requiring that Φ_0 be extremised. The result is the same as in Eq. (5.6) except that μ is constant, making the gap vary with q in contrast to the single channel picture where the gap had the same magnitude for all $q < 2/a$. With the form of the gap, we may then evaluate the sum over $\mathbf{q}$, allowing us to split the energy contributions into the BCS grand potential (the first term) and N_q–dependent communal correction that arises from the changing magnitude of the gap. For the physically realizable values of N_q, the static grand potential is minimized at $N_q = 1$, the standard BCS result. We therefore turn to address the contributions from the oscillating channels to determine whether they can drive communal pairing with $N_q > 1$.

5.3.2 Finite Ω plasma

Having determined the static channel contribution, we may now consider the effect of fluctuations in $\Omega \neq 0$ channels. We consider transitions of a Cooper pair from a stable static channel to a spontaneously decaying oscillating channel to obtain the occupation probability of an oscillating channel as $\Phi_{\mathbf{q}}\left(\left|\Delta_{\mathbf{q},\Omega}\right|\right)/(\Phi_{\mathbf{q}}\left(\left|\Delta_{\mathbf{q},0}\right|\right)+\Gamma^{\mathrm{sd}}_{\mathbf{q},\Omega})$. The modification to the mean-field partition function accounting for the short-lived excitations is then

$$\begin{aligned}\mathscr{Z}_{\Omega\neq 0} &= 1+\sum_{\mathbf{q},\Omega\neq 0}\frac{\Phi_{\mathbf{q}}\left(\left|\Delta_{\mathbf{q},\Omega}\right|\right)}{\Phi_{\mathbf{q}}\left(\left|\Delta_{\mathbf{q},0}\right|\right)+\Gamma^{\mathrm{sd}}_{\mathbf{q},\Omega}}\\ &\quad+\frac{1}{2!}\left(\sum_{\mathbf{q},\Omega\neq 0}\frac{\Phi_{\mathbf{q}}\left(\left|\Delta_{\mathbf{q},\Omega}\right|\right)}{\Phi_{\mathbf{q}}\left(\left|\Delta_{\mathbf{q},0}\right|\right)+\Gamma^{\mathrm{sd}}_{\mathbf{q},\Omega}}\right)^2\\ &\quad+\cdots\\ &= \exp\left[\sum_{\mathbf{q},\Omega\neq 0}\frac{\Phi_{\mathbf{q}}\left(\left|\Delta_{\mathbf{q},\Omega}\right|\right)}{\Phi_{\mathbf{q}}\left(\left|\Delta_{\mathbf{q},0}\right|\right)+\Gamma^{\mathrm{sd}}_{\mathbf{q},\Omega}}\right].\end{aligned} \tag{5.11}$$

The 1 accounts for the situation where no such excitations are present, the second term for when a single channel is excited, the third for when two are simultaneously excited and so on.

The form of the grand potential may be taken from Eq. (5.5) and the spontaneous decay rate from Subsection 5.2.2. In order to evaluate the sums, it is necessary to express the gap magnitudes

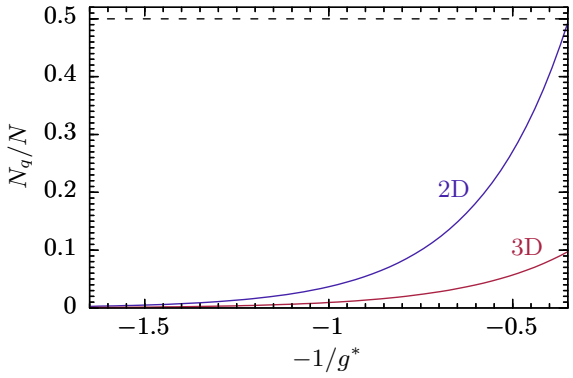

Fig. 5.1 Plot of the ratio of N_q to N as $N \to \infty$ as a function of dimensionless interaction strength g^* in 2D (blue) and 3D (red). In 2D, $-\frac{1}{g^*} = -\frac{1}{2}\ln k_F a$ while in 3D, $-\frac{1}{g^*} = \frac{3\pi}{8k_F a_s}$. Interaction strength increases from left to right. The dotted black line indicates the theoretical maximum of $\frac{N_q}{N} = \frac{1}{2}$.

explicitly in terms of $\mathbf{q}$ and Ω. Once again, we extremise the grand potential with respect to the $\Delta_{\mathbf{q},\Omega}$ to obtain $\left|\Delta_{\mathbf{q},\Omega}\right|^2 = |\Delta_{\mathbf{q}}|^2 - \Omega/ma^2$, which also allows us to explicitly compute the upper limit on Ω as $ma^2\Omega_M = \sqrt{8(1+ma^2\mu) - a^2q^2(1+2ma^2\mu)} - 2$, which is positive for $qa < 2$, the region we are interested in. From these relations we see that strong interactions, low a, drive oscillations of the gap.

With all this in place, we may now perform the summations to obtain the contribution to the partition function as

$$\mathscr{Z}_{\Omega\neq 0} = \exp\left[\frac{2L^2\beta}{3\pi^2 ma^4}\left(F(1) - F\left(1 - \frac{\pi N_q a^2}{L^2}\right)\right)\right], \tag{5.12}$$

where

$$F(x) = \frac{1+x\left(1+2ma^2\mu\right)\left(2\sqrt{1+x\left(1+2ma^2\mu\right)}-3\right)}{1+2ma^2\mu}$$

is a dimensionless function of the dimensionless variable x characterising the N_q dependence of this part of the partition function. The term in the exponential is positive for $1 < N_q < 1 + L^2/\pi a^2$, that is, for all accessible values of N_q, corresponding to an increase in the number of accessible microstates and thus an entropically driven decrease in the grand potential. The presence of temporally oscillating modes thus contributes an entropic term to the grand potential, increasing the number of accessible microstates and thereby reducing the grand potential. Qualitatively similar behaviour may be obtained in 3D.

5.3.3 Optimizing N_q

With the grand potential in place, we are well-positioned to determine N_q. Combining the static and oscillating contributions of Eq. (5.10) and Eq. (5.12) gives Φ as a function of N_q, which may then be minimized to obtain the optimal number of stabilised communal pairing channels as

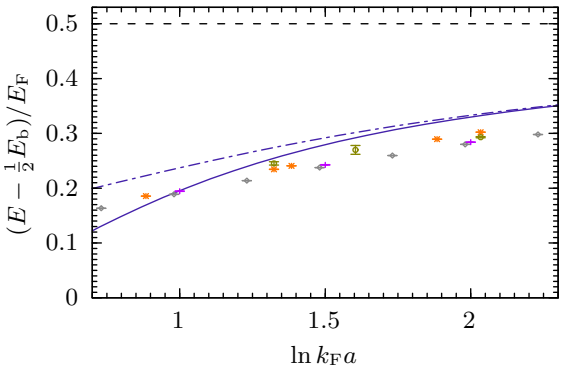

Fig. 5.2 Plot of energy against $\ln k_F a$. The dashed line shows the BCS mean-field result, the dotted-dashed line shows the result obtained from treatment of Gaussian gap fluctuations using the T-matrix method and the solid line shows the T-matrix results with our communal correction. Various quantum Monte Carlo results are shown for comparison. The communal correction is seen to make up for a significant portion of the discrepancy between the T-matrix and Monte Carlo results at intermediate interaction strengths.

$$N_q = 1 + \frac{2N}{k_F^2 a^2} - \frac{\pi(32+\pi)N}{128(1+2ma^2\mu)k_F^2 a^2},$$

that is, slightly fewer than the maximum permitted. The BCS limit of $N_q = 1$ or, in the thermodynamic limit, $N_q/N = 0$, is recovered in the weakly interacting limit of $k_F a \to \infty$. We expect the above expression to be most correct in the regime where the scattering length a is comparable to or less than the system size L so that $N_q > 2$, with the BCS limit being a good description for even weaker interactions. The key role played by the temporal fluctuations here in determining the width in momentum space, and thus the real space structure, of the superconducting gap means that communal pairing in spin-balanced systems emerges as order by disorder.

The grand potential in 3D exhibits qualitatively similar behaviour, favouring $N_q = 1$ if not for the addition of the temporal fluctuation term, which instead promotes near maximal N_q provided interactions are weak, that is $k_F a_s \to 0^-$.

The emergence of communal pairing and maximisation of N_q is shown in Fig. 5.1, with N_q increasing smoothly as a function of the scattering length in both 2D and 3D. This is a marked difference from BCS theory which presupposes $N_q = 1$ at all interaction strengths. For ease of comparison, we have chosen to plot N_q as a function of the dimensionless interaction strength $g^* = \frac{Nv_0}{E_F}$ where v_0 is the inverse of the first term in the regularisation Eq. (5.3), so $-\frac{1}{g^*} = -\frac{1}{2}\ln k_F a$ in 2D while in 3D, $-\frac{1}{g^*} = \frac{3\pi}{8k_F a_s}$. The effect is stronger in 2D compared to 3D due to fluctuations being stronger in 2D.

5.3.4 Adding gap fluctuations

we have shown how temporal fluctuations and concomitant expansion of the phase space entropically stabilise a communal state. These considerations are constitute a nontrivial extension of the original BCS theory that is nevertheless still a mean-field approach, and is therefore orthogonal to the usual treatment of Gaussian fluctuations of the order parameter, with which the T-matrix approach has had much success

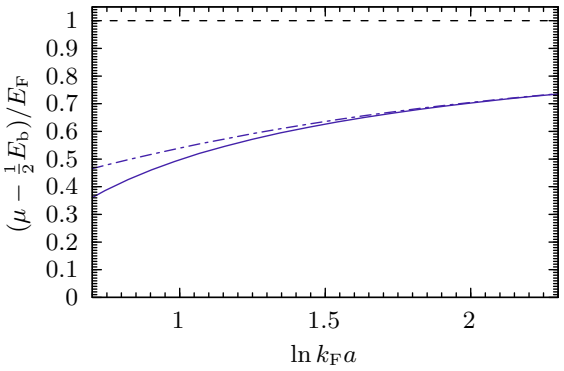

Fig. 5.3 Plot of chemical potential against $\ln k_F a$. The dashed line shows the BCS mean-field result, the dotted-dashed line shows the result obtained from treatment of Gaussian gap fluctuations using the T-matrix method and the solid line shows the T-matrix results with our communal correction.

[84]. It is therefore instructive to consider both sources of orthogonal fluctuation simultaneously by adding the difference between our obtained communal results and the traditional BCS mean field to the T-matrix results.

This is shown in Fig. 5.2 where we have plotted internal energy per particle against the interaction parameter $\ln k_F a$. The BCS mean field result is constant at 0.5, as seen by the dashed line, while the effects of Gaussian fluctuation of the order parameter obtained via the T-matrix approach are shown by the dotted-dashed line and are seen to consistently overestimate the energy calculated by quantum Monte Carlo methods [93, 94, 64, 78]. This disparity has previously been postulated as the GMB effect or beyond-quadratic fluctuations of the order parameter [84]. Adding our correction to the T-matrix results gives the solid line which comes closer to the Monte Carlo results, particularly around $1 < \ln k_F a < 2$. Furthermore, the quantum Monte Carlo results are more reliable in the intermediate interaction regime than the weakly interacting regime as the superconducting correlation length becomes smaller than the simulation cell length, making a correction in this intermediate regime particularly significant. We therefore contend that communal effects too may play an important role in the ground state. The overshoot at $\ln k_F a < 1$ is due to the aforementioned breakdown of assumptions at high interaction strength.

5.3.5 Connection to BEC-BCS crossover

The increase in extent of communal pairing N_q and concomitant width of the gap in momentum space with increasing interaction strength points to a connection between communal superconductivity and the BEC state. The communal pairing state comprises many tightly bound, spatially localised Cooper pairs whose corresponding gap parameter is spread out in momentum space, analogous to the BEC state that comprises many tightly bound pairs of fermions. To probe this connection, we look to the chemical potential. Following the prescription of Subsection 5.2.1, we solve for μ and obtain

$$\frac{\mu}{E_F} = 1 - \frac{1}{k_F^2 a^2} - \frac{8}{3\pi k_F^3 a^3} + \mathcal{O}\left(\frac{1}{k_F^5 a^5}\right).$$

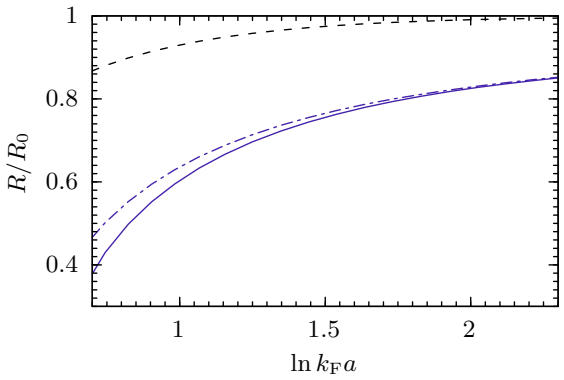

Fig. 5.4 Plot of radius of a trapped interacting Fermi gas R relative to the radius of a trapped noninteracting Fermi gas R_0 against $\ln k_F a$. The dashed line shows the BCS mean-field result, the dotted-dashed line shows the result obtained from treatment of Gaussian gap fluctuations using the T-matrix method and the solid line shows the T-matrix results with our communal correction.

The first two terms are the BCS solution so the communal pairing correction is readily isolated as a reduction of the chemical potential, as seen in Fig. 5.3. Starting from the non-interacting limit where $\mu = E_F$ as predicted by both BCS and communal pairing theory, as interactions get stronger μ decreases more quickly in communal pairing theory than in traditional pairing theory. The trends established in the communal state points towards a smooth evolution into the BEC regime, with a smooth confinement of more Cooper pairs with tighter spatial extent. The reduction of chemical potential persists even when incorporating the T-matrix analysis.

This variation of chemical potential with interaction strength may be verified directly by experiment, for example by considering the radius of a trapped ultracold atomic gas. In the local density approximation, the chemical potential μ and density n are related by $\mu \propto n^\gamma$ for some positive γ [38] and so the radius of the trapped gas R is where the local chemical potential vanishes, $\mu(R) \equiv \mu - V(R) = 0$ where $V(\mathbf{r})$ is the trapping potential. The radius of the trapped gas is thus a direct measure of the chemical potential by the relation $R \propto \sqrt{\mu}$. The full variation is shown in Fig. 5.4 where we see the change in radius is significant and should be readily observable in a cold atom gas.

5.4 Discussion and conclusions

We have demonstrated the importance of communal corrections to the BCS theory by increasing variational freedom to include multiple superconducting modes. Partial occupancy of the temporally oscillating modes drive communal ordering of the superconducting gap, with each nonzero gap mode corresponding to a Cooper pair of net momentum $\mathbf{q}$ variationally lowering the grand potential, resulting in a favouring of multiple nonzero gap modes. Widening of the gap in momentum space, and the concomitant confinement of the Cooper pairs in real space with increasing interaction strength, points to a connection between communal superconductivity and the BEC-BCS crossover. Fluctuations of the gap itself were incorporated through the T-matrix analysis [84] resulting in a favourable comparison of the system energy with quantum Monte Carlo results.

The analysis focuses on how the partial occupancy of the temporal oscillating superconducting gap modes drive the emergence of communal order. This partial occupancy is driven by quantum fluctuations,

that is by the uncertainty principle rather than temperature and so persist down to zero temperature where they affect the structure of the gap. We neglected the effect of density fluctuations that result in the GMB correction [19, 51, 21, 20, 95, 96] as it simply decouples from the superconducting analysis and reduces the superconducting gap [19, 21, 20]. Magnetic fluctuations were neglected as these are small in spin-balanced systems.

A significant experimental consequence of communal pairing is the variation of chemical potential with scattering length, which may potentially be observed in the radius of trapped cold gases. In addition, other experimental techniques such as radio-frequency spectroscopy [97, 98] that can directly probe the chemical potential. This reduction of the chemical potential compared to the BCS prediction may contribute to the persistent overestimation of the chemical potential by numerical methods compared to direct experimental measurements, such as those by the Jochim group [99], with the magnitude of this mismatch being particularly well described by communal pairing theory near the unitarity limit of $\ln k_{\mathrm{F}} a \approx 1$, where interactions are sufficiently strong for effects to be visible beyond experimental uncertainty but still within the range of validity of the theory presented.

Another possible experimental signature is that the spatial structure of the superconducting gap should change with the scattering length, from isotropic in the weakly interacting limit to strongly confined in real space as interactions get stronger and the system approaches the BEC limit. This may be investigated in cold atomic gases, where control of the scattering length is well established [97, 98, 100], for example using angle-resolved photoemission spectroscopy [101]. The momentum-space structure of the gap could also be probed directly using Bogoliubov quasiparticle interference imaging [102]. In 2D, the analysis predicts that the superconducting gap has a width in momentum space that is inversely proportional to the scattering length, $q_{2\mathrm{D}} = \frac{2}{a}$ at weak interactions with $k_{\mathrm{F}} a < 2$. In 3D, for weak interactions $k_{\mathrm{F}} a_{\mathrm{s}} \to 0^{-}$, the width is predicted to follow $q_{(3\mathrm{D})} \propto k_{\mathrm{F}} \mathrm{e}^{\pi/2 k_{\mathrm{F}} a_{\mathrm{s}}}$. However, we have demonstrated that low dimensionality promotes a higher N_q and so the experimental verification might be more straightforward in 2D systems. The additional pairing channels may also be visible through a range of retroreflected hole momenta in Andreev reflection experiments.

Chapter 6

Concluding remarks

Fermionic condensed matter systems have proven to be fertile ground for theorists and experimentalists alike, giving rise to both a wealth of theoretical discourse and cutting-edge devices. This thesis performed a detailed study of a general fermionic system with attractive point interactions, a theoretical model that has gathered much attention, and pushed the envelope a step further, not so much by adding complexity to the model but by insisting on not oversimplifying more than strictly necessary. In doing this it should be understood that the results so derived and detailed in the preceding chapters are foundational, and so advance the understanding of superconductivity in general.

The thesis began by considering additional degrees of variational freedom of a spin-imbalanced Fermi gas, the communal pairing indices $N_\uparrow$ and $N_\downarrow$, building on the foundational BCS theory [4] and FFLO theory [7, 8] where, in the language of communal pairing theory, the pairing indices $N_\uparrow = 1$ and $N_\downarrow = 1$. These indices N_σ have the physical interpretation of denoting the number of Cooper pairs a fermion of spin $-\sigma$ is shared by, that is the number of momentum states of spin σ a particular state of spin $-\sigma$ has nontrivial superconducting correlations with, or the number of choices of fermion states with which a fermion of spin$-\sigma$ may be bound. Thus, the key paradigm shift here has been the idea that a particular fermion may exist in a superposition of Cooper pairs, a consideration that earlier theories have not at all addressed. As recounted in the previous chapters and in published papers [1], this idea has immediate theoretical and experimental consequences; firstly, since $N_\uparrow$ and $N_\downarrow$ are variational parameters, their introduction cannot increase the energy of the pairing state as compared to the FFLO state and secondly, their taking non-unit values indicates a spreading out of the gap parameter in momentum space. These measurable consequences lead inevitably to the conclusion that the traditional view of superconducting pairing as occuring at very discrete and specific pairing momenta must be revised, and the communal pairing picture with its quantum-mechanically widened gap parameter goes a step further in providing an accurate description of the superconducting ground state.

High quality quantum Monte Carlo and exact diagonalisation calculations were undertaken to provide orthogonal and independent corroboration of the new communal pairing theory, and the results obtained broadly agree with the theoretical predictions [2]. This further establishes communal pairing theory as an improvement over FFLO theory and provides a clear impetus for both future experimental verification

and further theoretical work. The theoretical and numerical foundation laid with the introduction of communal pairing theory as has been derived here may also go some way to explaining discrepancies in prior experimental and numerical work, such as the chemical potential of 2D Fermi gases being consistently lower [99] than that predicted by older quantum Monte Carlo work [**?**], or in the large momentum space width of the condensate fraction observed in 1D DMC studies [103] that has thus far remain unremarked upon.

The central paradigm shift, that a fermion may be involved in more than one Cooper pair, was applied back to a fresh analysis of spin-balanced Fermi gases as these are easier to obtain experimentally. It was subsequently found that quantum fluctuations drive the formation of a communal-type ground state, which has experimental ramifications of its own [3]. The key observable, a widening in momentum space of the superconducting gap, has also been connected to the evolution of the Fermi gas across the BEC-BCS crossover. While the evolution of superconductivity and superfluidity with interaction strength has been well-discussed, this marks the first time that the crossover has been connected to the momentum-space structure of the gap.

While every effort has been made to ensure that the work undertaken was comprehensive, it is natural that opportunities for further work arise. For example, and has been mentioned previously, direct and convincing experimental evidence for the communal state is currently lacking, and we have detailed potential experiments in preceding chapters. Further work might also be done theoretically, for example adapting the language of the theory from the fermion gas description used to band theory, better describing solid-state materials. From there further extensions are possible such as considering multiband pairing and its potential effects, particularly when the Fermi surfaces are distorted by effects beyond the simple spin-imbalance.

Another avenue for further work would be to add complexity to the existing model in line with real material considerations. For example, adding a spin-orbit coupling term would be pertinent to many material systems, and a mass-imbalance would be applicable to a particle-physics context looking at colour superconductivity. The effects of a Zeeman field term would also be of potential experimental interest as a magnetic field is easily controlled and measured, and would be the immediate choice for setting up a spin-imbalance to start with.

References

[1] D. C. W. Foo, T. M. Whitehead and G. J. Conduit. *EPL*, 126(6), 2019.

[2] D. C. W. Foo and G. J. Conduit. *Phys. Rev. A*, 100(063602), 2019.

[3] Submitted for publication.

[4] J. Bardeen, L. N. Cooper, and J. R. Schrieffer. *Phys. Rev.*, 106(1):162–164, 1957.

[5] H. K. Onnes. *Comm. Phys. Lab. Univ. Leiden*, 120b, 1911.

[6] H. K. Onnes. *Comm. Phys. Lab. Univ. Leiden*, 122b, 1911.

[7] P. Fulde and R. A. Ferrell. *Phys. Rev.*, 135, 1964.

[8] A. I. Larkin and Y. N. Ovchinnikov. *Sov. Phys. JETP*, 20(762), 1965.

[9] Y. Matsuda and H. Shimahara. *J. Phys. Soc. Jpn.*, 76:051005, 2007.

[10] X. Shang L. Zhang, Y. Ge and Y. Gao. *Mod. Phys. Lett. B*, 33:1950082, 2019.

[11] M. W. Zwierlein, A. Schirotzek, C. H. Schunck, and W. Ketterle. *Science*, 311:492, 2006.

[12] Y. A. Liao, A. S. C. Rittner, T. Paprotta, W. Li, G. B. Partridge, R. G. Hulet, S. K. Baur and E. J. Mueller. *Nature*, 467:567–569, 2010.

[13] R. Lortz, Y. Wang, A. Demuer, P. H. M. Böttger, B. Bergk, G. Zwicknagl, Y. Nakazawa, and J. Wosnitza. *Phys. Rev. Lett.*, 99(18):187002, 2007.

[14] R. Beyer, B. Bergk, S. Yasin, J. A. Schlueter and J. Wosnitza. *Phys. Rev. Lett.*, 109(2):027003, 2012.

[15] G. Koutroulakis, H. Kühne, J. A. Schlueter, J. Wosnitza and S. E. Brown. *Phys. Rev. Lett.*, 116(6):067003, 2016.

[16] S. Sugiura, T. Isono, T. Terashima, S. Yasuzuka, J. A. Schlueter and S. Uji. *npj Quantum Mat.*, 4(7), 2019.

[17] S. V. Mironov, D. Y. Vodolazov, Y. Yerin, A. V. Samokhvalov, A. S. Mel'nikov and A. Buzdin. *Phys. Rev. Lett.*, 121:077002, 2018.

[18] L. N. Cooper. *Phys. Rev.*, 4(104):1189, 1956.

[19] L. P. Gor'kov and T. K. Melik-Barkhudarov. *JETP*, 13(5), 1961.

[20] D. S. Petrov, M. A. Baranov, and G. V. Shlyapnikov. *Phys. Rev. A*, 67(031601), 2003.

[21] H. Caldas and M. A. Continentino. *J. Phys. B*, 46(155301), 2013.

[22] R. Casalbuoni and G. Nardulli. *Rev. Mod. Phys.*, 76(263), 2004.

[23] Z. Dai, Y.-H. Zhang, T. Senthil, and P. Lee. *arXiv:1802.03009*, 2018.

[24] Y. Wang, S. D. Edkins, M. H. Hamidian, J. C. S. Davis, E. Fradkin, and S. A. Kivelson. *arXiv:1802.01582*, 2018.

[25] D. F. Agterberg and H. Tsunetsugu. *Nature Physics*, 4(6), 2009.

[26] R. Soto-Garrido and E. Fradkin. *Phys. Rev. B*, 89(165126), 2014.

[27] D. F. Agterberg and J. Garaud. *Phys. Rev. B*, 91(104512), 2015.

[28] E. Gubankova, W. V. Liu and F. Wilczek. *Phys. Rev. Lett.*, 91(032001), 2003.

[29] W. V. Liu and F. Wilczek. *Phys. Rev. Lett.*, 90(047002), 2003.

[30] M. M. Forbes, E. Gubankova, W. V. Liu, and F. Wilczek. *Phys. Rev. Lett.*, 94(017001), 2005.

[31] E. Gubankova, E. G. Mishchenko, and F. Wilczek. *Phys. Rev. Lett.*, 94(110402), 2005.

[32] A. M. Clogston. *Phys. Rev. Lett.*, 9(6):266–267, 1962.

[33] C. Lobo, A. Recati, S. Giorgini, and S. Stringari. *Phys. Rev. A*, 97(200403), 2006.

[34] A. Recati, C. Lobo, and S. Stringari. *Phys. Rev. A*, 78(023633), 2008.

[35] I. Bausmerth, A. Recati, and S. Stringari. *Phys. Rev. A*, 79(43622), 2009.

[36] T. M. Whitehead and G. J. Conduit. *Phys. Rev. B*, 97(014502), 2018.

[37] R. Needs, M. Towler, N. Drummond and P. López Ríos. CASINO User's Guide Version 2.13 (2015).

[38] W. Ketterle and M. W. Zwierlein. *arXiv:0801.2500*, 2008.

[39] S. K. Adhikari. *Am. J. Phys.*, 54(362), 1986.

[40] B. J. Verhaar, J. P. H. W. van den Eijnde, M. A. J. Voermans and M. M. J. Schaffrath. *J. Phys. A: Math. Gen.*, 17(595), 1984.

[41] T. M. Whitehead, L. M. Schonenberg, N. Kongsuwan, R. J. Needs and G. J. Conduit. *Phys. Rev. A*, 93(042702), 2016.

[42] W. M. C. Foulkes, L. Mitas, R. J. Needs and G. Rajagopal. *Rev. Mod. Phys.*, 73(33), 2001.

[43] D. M. Ceperley, G. V. Chester and M. H. Kalos. *Phys. Rev. B*, 16(7), 1977.

[44] N. Metropolis, A. W. Rosenbluth, M. N. Rosenbluth, A. H. Teller and E. Teller. *J. Chem. Phys.*, 21(6):1087–1092, 1953.

[45] I. Kosztin, B. Faber and K. Schulten. *Am. J. Phys*, 64(633), 1996.

[46] R. J. Needs, M. D. Towler, N. D. Drummond and P. López Ríos. *J. Phys. Condens. Matter*, 22(023201), 2010.

[47] G. C. Wick. . *Phys. Rev.*, 96(1124), 1954.

[48] J. R. Trail. *Phys. Rev. E*, 77(016703), 2008.

[49] J. Voit. *The Statistical Mechanics of Financial Markets*. Springer-Verlag, 2003.

[50] J. R. Trail. *Phys. Rev. E*, 77(016704), 2008.

[51] L. Pisani, A. Perali, P. Pieri, and G. Calvanese Strinati. *Phys. Rev. B*, 97(014528), 2018.

[52] J. A. Bowers and K. Rajagopal. *Phys. Rev. D*, 66(065002), 2002.

[53] J. A. Kok and W. H. Keesom. *Physica*, 4(835), 1937.

[54] C. A. Reynolds, B. Serin and L. B. Nesbitt. *Phys. Rev.*, 84(691), 1951.

[55] M. Horowitz, A. A. Silvidi, S. F. Malaker and J. G. Daunt. *Phys. Rev.*, 88(1182), 1952.

[56] F. Chevy. *Phys. Rev. A*, 74(063628), 2006.

[57] R. Combescot and S. Giraud. *Phys. Rev. Lett.*, 101(050404), 2008.

[58] P. Massignan, M. Zaccanti, and G. M. Bruun. *Rep. Prog. Phys.*, 77(034401), 2014.

[59] L. M. Schonenberg and G. J. Conduit. *Phys. Rev. A*, 95(013633), 2017.

[60] R. Maezono, P. López Ríos, T. Ogawa and R. J. Needs. *Phys. Rev. Lett.*, 110(216407), 2013.

[61] T. M. Whitehead, M. H. Michael and G. J. Conduit. *Phys. Rev. B*, 94(035157), 2016.

[62] N. D. Drummond, R. J. Needs, A. Sorouri and W. M. C. Foulkes. *Phys. Rev. B*, 78(125106), 2008.

[63] D. Frenkel. *Eur. Phys. J. Plus*, (128: 10), 2013.

[64] A. Galea, H. Dawkins, S. Gandolfi and A. Gezerlis. *Phys. Rev. A*, 93(023602), 2016.

[65] G. E. Astrakharchik, J. Boronat, J. Casulleras and S. Giorgini. *Phys. Rev. Lett*, 93(200404), 2004.

[66] A. Bulgac, M. M. Forbes and A. Schwenk. *Phys. Rev. Lett.*, 97(020402), 2006.

[67] M. M. Forbes, E. Gubankova, W. V. Liu and F. Wilczek. *Phys. Rev. Lett.*, 94(017001), 2005.

[68] B. S. Chandrasekhar. *Appl. Phys. Lett.*, 1(7), 1962.

[69] M. Casula and D. M. Ceperley. *Phys. Rev. Lett.*, 97(020402), 2006.

[70] P. O. Bugnion, J. A. Lofthouse and G. J. Conduit. *Phys. Rev. Lett.*, 111(045301), 2013.

[71] H. Shimahara. *J. Phys. Soc. Japan*, 67(736), 1998.

[72] C. Mora and R. Combescot. *EPL*, 66(833), 2004.

[73] W. D. Parker, J. W. Wilkins, R. G. Hennig. *Phys. Status Solidi B*, 248(2), 2011.

[74] R. M. Lee, G. J. Conduit, N. Nemec, P. López Ríos, and N. D. Drummond. *Phys. Rev. E*, 83(066706), 2011.

[75] J. Vrbik and S. M. Rothstein. *Int. J. Quantum Chem.*, 29(461), 1986.

[76] E. Altman, E. Demler, and M. D. Lukin. *Phys. Rev. A*, 70(013603), 2004.

[77] M. J. H. Ku, A. T. Sommer, L. W. Cheuk, and M. W. Zwierlein. *Science*, 335(563), 2012.

[78] L. M. Schonenberg, P. C. Verpoort and G. J. Conduit. *Phys. Rev. A*, 96(023619), 2017.

[79] J. Eisenstein. *Rev. Mod. Phys.*, 26(277), 1954.

[80] G. W. Webb, F. Marsiglio and J. E. Hirsch. *Physica C*, 514(17), 2015.

[81] M. I. Eremets and A. P. Drozdov. *Phys.-Usp*, 59(1154), 2016.

[82] R. N. Araújo and E. C. Andrade. *Phys. Rev. B*, 100(014510), 2019.

[83] G. M. Eliashberg. *Zh. Eksp. Teor. Fiz.*, 38(966), 1960.

[84] L. He, H. Lü, G. Cao, H. Hu and X. Liu. *Phys. Rev. A*, 92(023620), 2015.

[85] J. Carlson, S. Y. Chang, V. R. Pandharipande, and K. E. Schmidt. *Phys. Rev. Lett.*, 91(050401), 2003.

[86] A. Bulgac, J. E. Drut, and P. Magierski. *Phys. Rev. A*, 78(023625), 2008.

[87] J. E. Baarsma, K. B. Gubbels, and H. T. C. Stoof. *Phys. Rev. A*, 82(013624), 2010.

[88] J. Wang, Y. Che, L. Zhang, Q. Chen. *Sci. Rep.*, 7(39783), 2017.

[89] R. Dasgupta. *Phys. Rev. A*, 82(063607), 2010.

[90] B. Marcelis, B. Verhaar and S. Kokkelmans. *Phys. Rev. Lett.*, 100(153201), 2008.

[91] P. Zhang, P. Naidon and M. Ueda. *Phys. Rev. Lett.*, 103(133202), 2009.

[92] N. Arunkumar, A. Jagannathan and J. E. Thomas. *Phys. Rev. Lett.*, 122(040405), 2019.

[93] G. Bertaina and S. Giorgini. *Phys. Rev. Lett.*, 106(110403), 2011.

[94] H. Shi, S. Chiesa and S. Zhang. *Phys. Rev. A*, 92(033603), 2015.

[95] M. A. Resende, A. L. Mota, R. L. S. Farias, and H. Caldas. *Phys. Rev. A*, 86(033603), 2012.

[96] Z. Q. Yu and L. Yin. *Phys. Rev. A*, 82(013605), 2010.

[97] B. Mukherjee, P. B. Patel, Z. Yan, R. J. Fletcher, J. Struck and M. W. Zwierlein. *Phys. Rev. Lett.*, 122(203402), 2019.

[98] Z. Yan, P. B. Patel, B. Mukherjee, R. J. Fletcher, J. Struck and M. W. Zwierlein. *Phys. Rev. Lett.*, 122(093401), 2019.

[99] I. Boettcher, L. Bayha, D. Kedar, P. A. Murthy, M. Neidig, M. G. Ries, A. N. Wenz, G. Zürn, S. Jochim and T. Enss. *Phys. Rev. Lett.*, 116(045303), 2016.

[100] B. Mukherjee, Z. Yan, P. B. Patel, Z. Hadzibabic, T. Yefsah, J. Struck and M. W. Zwierlein. *Phys. Rev. Lett.*, 118(123401), 2017.

[101] P. T. Brown, E. Guadado-Sanchez, B. M. Spar, E. W. Huang, T. P. Devereaux and W. S. Bakr. *Nature Physics*, 16(26), 2020.

[102] R. Sharma, S. D. Edkins, Z. Wang, A. Kostin, C. Sow, Y. Maeon, A. P. Mackenzie, J. C. Séamus Davis and V. Madhavan. *Proc. Natl. Acad. Sci. U.S.A.*, 117(10), 2020.

[103] M. Casula, D. M. Ceperley and E. J. Mueller. *Phys. Rev. A*, 78(033607), 2008.